



1 **Dust storms from the Taklamakan Desert significantly darken snow**  
2 **surface on surrounding mountains**

3 Yuxuan Xing<sup>1</sup>, Yang Chen<sup>1</sup>, Shirui Yan<sup>1</sup>, Tenglong Shi<sup>1</sup>, Xiaoyi Cao<sup>1</sup>, Xiaoying Niu<sup>1</sup>,  
4 Dongyou Wu<sup>1</sup>, Jiecan Cui<sup>1,2</sup>, Xin Wang<sup>1,3</sup>, Wei Pu<sup>1</sup>

5 <sup>1</sup>Key Laboratory for Semi-Arid Climate Change of the Ministry of Education, College of Atmospheric  
6 Sciences, Lanzhou University, Lanzhou 730000, China

7 <sup>2</sup>Zhejiang Development & Planning Institute, Hangzhou 310030, China

8 <sup>3</sup>Institute of Surface-Earth System Science, Tianjin University, Tianjin 300072, China

9 *Correspondence to:* Wei Pu (puwei@lzu.edu.cn)

10



11 **Abstract**

12 The Taklamakan Desert (TD) is a major source of mineral dust emissions into the  
13 atmosphere. These dust particles have the ability to darken the surface of snow on the  
14 surrounding high mountains after deposition, significantly impacting the regional  
15 radiation balance. However, previous field measurements have been unable to capture  
16 the effects of severe dust storms accurately, and their representation on regional scales  
17 has been inadequate. In this study, we propose a modified remote-sensing approach that  
18 combines data from the Moderate Resolution Imaging Spectroradiometer (MODIS)  
19 satellite and simulations from the Snow, Ice, and Aerosol Radiative (SNICAR) model.  
20 This approach allows us to detect and analyze the substantial snow darkening resulting  
21 from dust storm deposition. We focus on three typical dust events originating from the  
22 Taklamakan Desert and observe significant snow darkening over an area  
23 of >2100, >600, and >630 km<sup>2</sup> in the Tien Shan, Kunlun, and Qilian Mountains,  
24 respectively. Our findings reveal that the impact of dust storms extends beyond the local  
25 high mountains, reaching mountains located approximately 1000 km away from the  
26 source. Furthermore, we observe that dust storms not only darken the snowpack during  
27 the spring but also in the summer and autumn seasons, leading to increased absorption  
28 of solar radiation. Specifically, the snow albedo reduction (radiative forcing) triggered  
29 by severe dust depositions is up to 0.028–0.079 (11–31.5 W m<sup>-2</sup>), 0.088–0.136 (31–49  
30 W m<sup>-2</sup>), and 0.092–0.153 (22–38 W m<sup>-2</sup>) across the Tien Shan, Kunlun, and Qilian  
31 Mountains, respectively. This further contributes to the aging of the snow, as evidenced  
32 by the growth of snow grain size. Comparatively, the impact of persistent but relatively  
33 slow dust deposition over several months during non-event periods is significantly  
34 lower than that of individual dust event. This highlights the necessity of giving more  
35 attention to the influence of extreme events on the regional radiation balance. Through  
36 this study, we gain a deeper understanding of how a single dust event can affect the  
37 extensive snowpack and demonstrates the potential of employing satellite remote-  
38 sensing to monitor large-scale snow darkening.

39 **1 Introduction**



40 High Mountain Asia (HMA), which includes the Tibetan Plateau (TP) and surrounding  
41 mountain ranges, holds the largest amount of glaciers and snow outside of the poles.  
42 This region is informally known as the “The Third Pole” and the “Asian Water Tower”  
43 (Yao et al., 2012, 2019) because of its extreme importance as a freshwater source, with  
44 approximately one billion people relying on the water and hydropower that the glaciers  
45 and snow across HMA regularly provide (Immerzeel et al., 2012; Mishra et al., 2018).  
46 The snow-covered area of HMA is a highly reflective natural surface that has a  
47 significant impact on the regional radiation balance (Cohen and Rind, 1991; Painter et  
48 al., 2012). Previous satellite- and ground-based observations have demonstrated that  
49 the mass and extent of the snow cover across HMA are rapidly declining owing to  
50 recent global warming (Bormann et al., 2018; Notarnicola et al., 2020; Pulliainen et al.,  
51 2020). Furthermore, growing evidence has indicated that light-absorbing particles  
52 (LAPs), such as mineral dust and black carbon (BC), can induce snow darkening effect  
53 when they are deposited on the snow surface (Wang et al., 2013; Qian et al., 2015; Dang  
54 et al., 2017; Huang et al., 2022; Niu et al., 2022; Réveillet et al., 2022). This snow  
55 darkening effect increases solar absorption and decreases snow albedo, resulting in  
56 enhanced snowmelt and an imbalance in the Asian Water Tower (Hadley and  
57 Kirchstetter, 2012; Dumont et al., 2014; He et al., 2017, 2018; Shi et al., 2021, 2022a,  
58 2022b; Cordero et al., 2022). Consequently, the snow-darkening effect plays a critical  
59 role in snow decline across HMA, thereby perturbing the climate system and impacting  
60 hydrological cycles (Kraaijenbrink et al., 2017, 2021; Sang et al., 2019; Shi et al., 2019;  
61 Zhang et al., 2020, 2021; Roychoudhury et al., 2022; Yang et al., 2022).

62 The Taklamakan Desert (TD) in southwestern Xinjiang, Northwest China, is the  
63 second-largest shifting sand desert on Earth and accounts for 42% of all dust emissions  
64 in East Asia (Chen et al., 2017a). Approximately 70.54 Tg of dust are emitted into the  
65 atmosphere annually, with the most intense dust events occurring in spring (Chen et al.,  
66 2017a). The dust in the Tarim Basin is predominantly redeposited onto nearby regions  
67 owing to the surrounding high mountains (Qiu et al., 2001; Sun et al., 2001; Shao and  
68 Dong, 2006). When the dust is uplifted above 4 km altitude, it may eventually settle on  
69 the snow surfaces across the surrounding high mountains, such as the Tien Shan and



70 Kunlun Mountains and subsequently induce a snow-darkening effect (Ge et al., 2014;  
71 Jia et al., 2015; Yuan et al., 2018). Furthermore, this dust is also transported eastward  
72 beyond the Tarim Basin and can be transported all the way to the Qilian Mountains via  
73 the westerly winds during spring and summer, thereby inducing a snow darkening effect  
74 in this distal region to the east of the TD (Dong et al., 2020; Han et al., 2022). Therefore,  
75 TD dust may have a profound effect on the regional radiative balance by darkening the  
76 snow across the high mountains surrounding the TD. This effect may subsequently  
77 accelerate snow melting and affect water resources for the 30+ million people living in  
78 the Xinjiang and Gansu provinces of China (Mishra et al., 2021).

79 Numerous field measurements have been undertaken in recent decades to investigate  
80 the dust content of snow/glaciers across the high mountains surrounding the TD, with  
81 measured dust contents generally varying from 1.4 to 110  $\mu\text{g g}^{-1}$  (Wake et al., 1994;  
82 Dong et al., 2009, 2014; Wu et al., 2010; Ming et al., 2016; Xu et al., 2016; Schmale et  
83 al., 2017; Zhang et al., 2018, 2021; Wang et al., 2019; Li et al., 2021, 2022). This  
84 abundance of dust particles has been found to induce a significant snow darkening  
85 effect across the high-mountain snowpack, thereby increasing its associated radiative  
86 forcing to 25.8–65.7  $\text{W m}^{-2}$ . Furthermore, the estimated natural dust-induced snow-  
87 darkening effect can be equivalent to that induced by BC, particularly during intense  
88 springtime dust events (Sarangi et al., 2020; Zhang et al., 2021). These findings  
89 effectively highlight the significance of the TD dust-induced snow darkening effect  
90 across the surrounding high mountains. In spite of these invaluable in situ findings,  
91 ground-based observations are poorly represented at the regional scale owing to limited  
92 spatial coverage and temporal discontinuity. Furthermore, these previous field  
93 measurements may not be able to capture severe dust emission and loading events,  
94 which are more likely to induce snow darkening than common dry and wet deposition  
95 processes (Dumont et al., 2020; Pu et al., 2021; Baladima et al., 2022).

96 Satellite remote sensing offers an effective way to overcome the limitations of ground-  
97 based measurements by providing a more comprehensive understanding of the LAP-  
98 induced impact on the regional radiative forcing of the snowpack (Skiles et al., 2018a).



99 For example, Painter et al. (2012) found that the instantaneous LAP-induced radiative  
100 forcing can exceed  $250 \text{ W m}^{-2}$  in the Hindu Kush-Himalaya region via an analysis of  
101 Moderate Resolution Imaging Spectroradiometer (MODIS) satellite data. Sarangi et al.  
102 (2020) further revealed that dust is the primary factor responsible for high-altitude snow  
103 darkening in the Hindu Kush–Himalaya region. Similarly, severe dust events from the  
104 Sahara can deposit dust on the snowpack across the European Alps and Caucasus  
105 Mountains (Di Mauro et al., 2015; Dumont et al., 2020), with this deposition inducing  
106 a radiative forcing of up to  $153 \text{ W m}^{-2}$  based on satellite retrievals in Europe. Dust  
107 deposition has also induced extensive snow darkening across the Upper Colorado River  
108 Basin in North America, particularly during extreme dust events (Skiles et al., 2016,  
109 2018b; Painter et al., 2017). These studies have demonstrated the effectiveness of  
110 employing satellite remote sensing to estimate the dust content of the snowpack and its  
111 associated radiative forcing. However, detecting natural dust deposition on the snow  
112 surfaces across high mountains surrounding the TD is still limited.

113 Here we investigate the impact of dust storms on snow albedo reduction and radiative  
114 forcing across the high mountains surrounding the TD. We first utilize MODIS satellite  
115 data and the Snow, Ice, and Aerosol Radiative (SNICAR) model to retrieve the dust  
116 content of the snowpack. We then capture three typical dust events that induced snow  
117 darkening in the Tien Shan, Kunlun, and Qilian Mountains, respectively. Finally, we  
118 analyze the spatial and altitudinal variations in dust-induced snow darkening and  
119 compare our retrievals with field measurements. Through remote sensing observations,  
120 we aim to provide a new view of the darkening effect of natural desert dust on the  
121 snowpack of the high mountains surrounding the TD.

## 122 **2 Methodology**

### 123 **2.1 Remote-sensing data**

124 We accessed two MODIS datasets, the surface reflectance (MOD09GA:  
125 <https://earthdata.nasa.gov>;  $500 \times 500 \text{ m}$  resolution) and aerosol optical depth (AOD;  
126 MCD19A2), to evaluate the impact of dust on snow albedo. MOD09GA is the daily  
127 surface reflectance product from the Terra satellite, which provides the reflectance data



128 for seven bands (band 1, 620–670 nm; band 2, 841–876 nm; band 3, 459–479 nm; band  
129 4, 545–565 nm; band 5, 1230–1250 nm; band 6, 1628–1652 nm; band 7, 2105–2155  
130 nm). Previous studies have indicated that the MODIS sensor on Terra is not affected by  
131 saturation on bright snow surfaces. As a result, it has the capability of detecting changes  
132 in reflectance in the visible (VIS) bands caused by dust in snow (Painter et al., 2012;  
133 Pu et al., 2019).

134 The daily averaged downward shortwave flux was obtained from the NASA Clouds  
135 and the Earth’s Radiant Energy System (CERES: <https://ceres.larc.nasa.gov>;  $1^\circ \times 1^\circ$   
136 resolution). The CERES data products take advantage of the synergy between  
137 collocated CERES instruments and spectral imagers, such as MODIS (Terra and Aqua)  
138 and the Visual Infrared Imaging Radiometer Suite (S-NPP and NOAA-20). We used the  
139 downward shortwave flux to estimate the daily averaged radiative forcing that was due  
140 to dust deposition on the snowpack. The Cloud-Aerosol Lidar with Orthogonal  
141 Polarization (CALIOP/CALIPSO) provided by NASA is able to detect the type and  
142 height of aerosols in the atmosphere (Huang et al., 2007; Han et al., 2022) and can  
143 therefore be used to identify the movement of dust storms over the high mountains  
144 surrounding the TD.

145 The Shuttle Radar Topography Mission (SRTM) digital elevation data, which possess  
146 a 90-m spatial resolution, were provided by NASA and downloaded from Google Earth  
147 Engine (<https://earthengine.google.com>). These data were used to correct the influence  
148 of topography on surface reflectance.

## 149 **2.2 Snow depth and wind data**

150 The snow depth data were provided by NASA and accessed from the Modern-Era  
151 Retrospective Analysis for Research and Applications, Version 2 (MERRA-2:  
152 <https://gmao.gsfc.nasa.gov>). The MERRA-2 snow depth product was selected because  
153 it has better accuracy than those from ERA-Interim, JJA-55, and ERA5 across HMA  
154 (Orsolini et al, 2019). The wind field data were obtained from the European Centre for  
155 Medium-Range Weather Forecasts (ECMWF) Reanalysis v5 (ERA5:  
156 <https://www.ecmwf.int>) owing to its superior performance in terms of its high spatial  
157 resolution and longer time span compared with other products (Copernicus Climate



158 Change Service, 2017). Here, we used ERA5 wind data at 700 hPa to describe the  
159 atmospheric circulation during the analyzed dust storms.

### 160 **2.3 Radiative-transfer model**

161 The SNICAR model is a two-stream radiative transfer model (Flanner et al., 2007, 2009)  
162 that has been widely used to simulate the spectral albedo of LAP-contaminated snow  
163 (Sarangi et al., 2019; Chen et al., 2021). The model includes snow properties such as  
164 snow depth and effective radius and accounts for the incident radiation at the surface  
165 and its spectral distribution, solar zenith angle, and the type and concentration of LAPs  
166 in the snowpack. In this study, dust optical parameters are taken from SNICAR defaults,  
167 where the refractive index is  $1.56 + 0.0038i$  at  $0.63 \mu\text{m}$  (Patterson et al., 1981). And a  
168 diameter bin of  $0.1\text{-}1 \mu\text{m}$  was selected according to the previous observations from  
169 Taklamakan Desert (Okada and Kai, 2004).

170 The Santa Barbara DISORT Atmospheric Radiative Transfer (SBDART) model is one  
171 of the most widely used models for simulating the surface solar irradiance in clear and  
172 cloudy sky conditions (Ricchiazzi et al., 1998). The SBDART model includes standard  
173 atmospheric models, cloud models, extraterrestrial source spectra, gas absorption  
174 models, standard aerosol models, and surface models. Here, we used the SBDART  
175 model to calculate the spectral surface solar irradiance, following the approach of Cui  
176 et al. (2021).

### 177 **2.4 Terrain correction**

178 The high mountains surrounding the TD have a complex terrain, such that the local  
179 solar zenith angle ( $\beta$ ) may differ from the MODIS-derived solar zenith angle ( $\theta_0$ ).  
180 Therefore, the topographic correction method should be used to derive  $\beta$  (Teillet et al.,  
181 1982; Negi and Kokhanovsky, 2011):

$$182 \cos \beta = \cos \theta_0 \cos \theta_T + \sin \theta_0 \sin \theta_T \cos (\phi_0 - \phi_T), \quad (1)$$

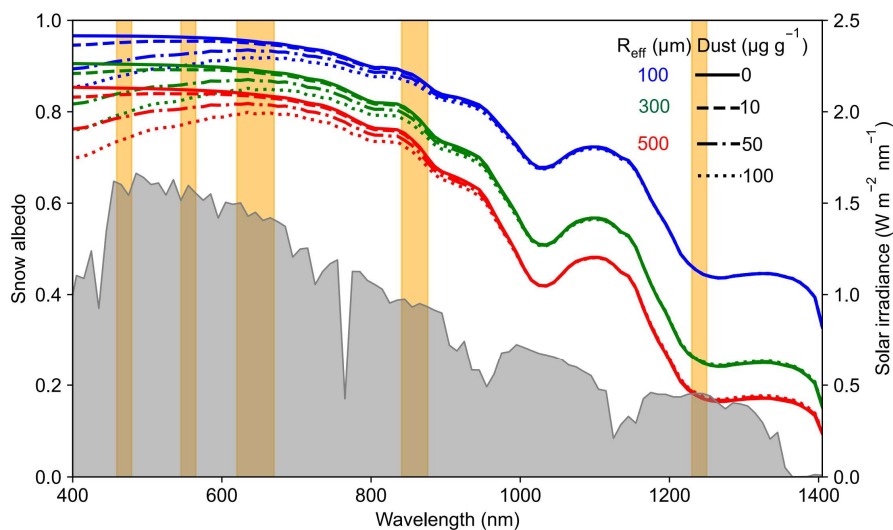
183 where  $\phi_0$  is the solar azimuth angle from MODIS, and  $\theta_T$  and  $\phi_T$  are the surface  
184 slope and aspect from SRTM, respectively. We then replace  $\theta_0$  with  $\beta$  in subsequent  
185 satellite retrievals.

### 186 **2.5 Snow properties retrieval**



187 The dust-contaminated spectral snow albedo is determined based on the dust content,  
188 snow grain size, snow depth, and solar zenith angle (Wiscombe and Warren, 1980). The  
189 dust content and snow depth primarily impact the snow albedo in the ultraviolet (UV)  
190 and VIS wavelengths, with a much smaller effect on snow albedo in the near infrared  
191 (NIR) wavelengths (Figure 1 and Figure S1). Conversely, the snow grain size and solar  
192 zenith angle primarily impact the snow albedo in the NIR wavelengths. The solar zenith  
193 angle and snow depth data are from MODIS Terra and MERRA-2, respectively. We  
194 used the SNICAR model to derive the quantitative snow grain size and dust content  
195 from the MODIS data. We then used the SBDART model to estimate the dust-induced  
196 snow albedo reduction and radiative forcing.

197



198

199 **Figure 1. Snow albedo spectra for different snow optical effective radius ( $R_{\text{eff}}$ ) and**  
200 **dust contents that were simulated using the SNICAR model. Orange bars denote**  
201 **MODIS bands, and the gray region represents the typical solar irradiance in HMA.**

202 The Snow-Covered Area and Grain size (SCAG) model is a spectral unmixing method  
203 that is widely used for identifying snow cover fraction (SCF) and snow optical effective  
204 radius ( $R_{\text{eff}}$ ), especially in complex mountain terrains (Painter et al., 2009, 2012; Rittger  
205 et al., 2013). The SCAG model retrieves the SCF and  $R_{\text{eff}}$  using all seven bands of the





206 MODIS reflectance data, which span the VIS to NIR range. It does not consider the  
 207 impact of LAPs. However, in our study, the dust content in snow is extreme high, which  
 208 will significantly reduce the VIS snow albedo in MODIS bands 1, 3, 4 (Figure 1). So,  
 209 the SCAG model will introduce a large bias in the resultant SCF and  $R_{\text{eff}}$  retrievals.  
 210 Furthermore, the reflectance of fine-grained dirty snow has been compared with that of  
 211 pure coarse-grained snow at short-wave infrared wavelengths, which include bands 6  
 212 and 7 (Bair et al., 2020). The extremely high dust content in this study therefore means  
 213 that the reflectance in MODIS bands 6 and 7 is not appropriate for snow property  
 214 retrieval. Instead, we used the reflectance data in MODIS bands 2 and 5 to unmix the  
 215 surface reflectance to derive SCF and  $R_{\text{eff}}$ , similar to the approach in Painter et al.  
 216 (2009). The surface reflectance at band  $i$  ( $R_{\text{band } i}^{\text{MODIS}}$ ) can be expressed as follows (Cui et  
 217 al., 2021):

$$218 \quad R_{\text{band } i}^{\text{MODIS}} = \frac{E_{\text{band } i} \times \text{SCF} \times R_{\text{band } i}^{\text{MODIS, snow}} + E_{\text{band } i} \times (1 - \text{SCF}) \times R_{\text{band } i}^{\text{soil}}}{E_{\text{band } i}}$$

$$219 \quad = \text{SCF} \times R_{\text{band } i}^{\text{MODIS, snow}} + (1 - \text{SCF}) \times R_{\text{band } i}^{\text{soil}}, \quad (2)$$

220 where  $R_{\text{band } i}^{\text{MODIS, snow}}$  and  $R_{\text{band } i}^{\text{soil}}$  represent the snow and soil reflectances at band  $i$ ,  
 221 respectively, with  $R_{\text{band } i}^{\text{soil}}$  taken from Siegmund and Menz (2005), and  $E_{\text{band } i}$  is the  
 222 solar irradiance at band  $i$ . The snow reflectance at band  $i$  ( $R_{\text{band } i}^{\text{MODIS, snow}}$ ) can be  
 223 expressed as

$$224 \quad R_{\text{band } i}^{\text{MODIS, snow}} = \left( \frac{R_{\text{band } i}^{\text{MODIS}} - (1 - \text{SCF}) \times R_{\text{band } i}^{\text{soil}}}{\text{SCF}} \right). \quad (3)$$

225 We then fit the SNICAR-simulated snow reflectance to the MODIS-derived snow  
 226 reflectance, which is expressed as either

$$227 \quad \text{RMSE} = \left( \frac{1}{2} (a \times (R_{\text{band } 2}^{\text{SNICAR, snow}} - R_{\text{band } 2}^{\text{MODIS, snow}})^2 + (R_{\text{band } 5}^{\text{SNICAR, snow}} - R_{\text{band } 5}^{\text{MODIS, snow}})^2) \right)^{\frac{1}{2}} \quad (4)$$

228 or

$$229 \quad \text{RMSE} = \left( \frac{1}{2} (a \times (R_{\text{band } 2}^{\text{SNICAR, snow}} - \left( \frac{R_{\text{band } 2}^{\text{MODIS}} - (1 - \text{SCF}) \times R_{\text{band } 2}^{\text{soil}}}{\text{SCF}} \right))^2) \right)^{\frac{1}{2}}$$



$$230 \quad + (R_{\text{band } 5}^{\text{SNICAR, snow}} - \left( \frac{R_{\text{band } 5}^{\text{MODIS}} - (1 - \text{SCF}) \times R_{\text{band } 5}^{\text{soil}}}{\text{SCF}} \right) )^2 )^{\frac{1}{2}}, \quad (5)$$

231 where RMSE is the root mean square error,  $R_{\text{band } i}^{\text{SNICAR, snow}}$  is the SNICAR-simulated  
 232 snow reflectance at band  $i$  (which is dependent on the  $R_{\text{eff}}$  and solar zenith angle, where  
 233 the solar zenith angle is derived from the MODIS data), and  $a$  is an empirical coefficient  
 234 (0.1–1 range). In this study,  $a$  was set to 0.1 to reduce the interference of dust on the  
 235 snow properties retrieval because a high dust content can influence the snow albedo at  
 236 band 2 (Figure 1). We can then derive SCF and  $R_{\text{eff}}$  by minimizing the RMSE (Painter  
 237 et al., 2009).

## 238 2.6 Dust content and snow albedo reduction retrieval

239 We fit the SNICAR-simulated snow reflectance to the MODIS-derived snow  
 240 reflectance in bands 3 and 4, which are the most sensitive to the dust content in snow,  
 241 following Pu et al. (2019) and Cui et al. (2021), which are expressed as either

$$242 \quad \text{RMSE} = \left( \frac{1}{2} \left( (R_{\text{band } 3}^{\text{SNICAR, snow}} - R_{\text{band } 3}^{\text{MODIS, snow}})^2 + (R_{\text{band } 4}^{\text{SNICAR, snow}} - R_{\text{band } 4}^{\text{MODIS, snow}})^2 \right) \right)^{\frac{1}{2}} \quad (6)$$

243 or

$$244 \quad \text{RMSE} = \left( \frac{1}{2} \left( \left( R_{\text{band } 3}^{\text{SNICAR, snow}} - \left( \frac{R_{\text{band } 3}^{\text{MODIS}} - (1 - \text{SCF}) \times R_{\text{band } 3}^{\text{soil}}}{\text{SCF}} \right) \right)^2 \right. \right. \\ 245 \quad \left. \left. + \left( R_{\text{band } 4}^{\text{SNICAR, snow}} - \left( \frac{R_{\text{band } 4}^{\text{MODIS}} - (1 - \text{SCF}) \times R_{\text{band } 4}^{\text{soil}}}{\text{SCF}} \right) \right)^2 \right) \right)^{\frac{1}{2}}, \quad (7)$$

246 where  $R_{\text{band } 3}^{\text{SNICAR, snow}}$  is a function of four factors: dust content,  $R_{\text{eff}}$ , snow depth, and  
 247 solar zenith angle. The latter three factors have been derived, leaving the dust content  
 248 as the only unknown. Therefore, the dust content can be retrieved by minimizing Eq.  
 249 (7). We assume that the derived dust content in this study accounts for the total light  
 250 absorption by all of the LAPs that are present in the snowpack. This is because our  
 251 study area is close to the Taklamakan Desert (TD), where large amounts of dust  
 252 accumulate on the snow surface annually. In contrast, anthropogenic activities and  
 253 biomass burning are rare, resulting in limited depositions of black carbon (BC) and  
 254 organic carbon (OC) (Fig. S8). Observations from snow and atmosphere have



255 confirmed this phenomenon (Wake et al., 1994; Huang et al., 2007). Therefore, our  
256 assumption is plausible.

257 The dust-induced broadband albedo reduction ( $\Delta\alpha$ ) can then be calculated as follows:

$$258 \Delta\alpha = \frac{\sum_{\lambda=300\text{nm}}^{\lambda=2500\text{nm}} E_{\lambda} (R_{\lambda}^{\text{SNICAR, pure-snow}} - R_{\lambda}^{\text{SNICAR, snow}}) \cdot \Delta\lambda}{\sum_{\lambda=300\text{nm}}^{\lambda=2500\text{nm}} E_{\lambda} \cdot \Delta\lambda}, \quad (8)$$

259 where  $E_{\lambda}$  represents the total solar irradiance at wavelength  $\lambda$  from the SBDART model,

260  $\Delta\lambda$  is 10 nm, and  $R_{\lambda}^{\text{SNICAR, pure-snow}}$  and  $R_{\lambda}^{\text{SNICAR, snow}}$  are the SNICAR-simulated pure

261 and polluted snow albedo, respectively. The dust-induced radiative forcing (RF) is  
262 calculated as follows:

$$263 \text{RF} = \Delta\alpha \cdot \text{SW}, \quad (9)$$

264 where SW is the downward shortwave flux, which is obtained from CERES.

265 The in situ dust content was not measured to verify the MODIS retrievals because of  
266 the challenging geographical conditions surrounding the TD. Nevertheless, Cui et al.  
267 (2021) verified a similar retrieval method and reported an uncertainty of less than ~40%  
268 over highly polluted snow. As noted above, the snow albedo reduction is mainly  
269 dependent on the dust content,  $R_{\text{eff}}$ , snow depth, and solar zenith angle. The  $R_{\text{eff}}$  and  
270 snow depth can be categorized as snow properties. We compared the dust content, snow  
271 properties, and solar zenith angle to discuss their contributions to the spatial variations  
272 in snow albedo reduction (Pu et al, 2019; Cui et al., 2021). The supplementary  
273 information contains a thorough derivation of this method.

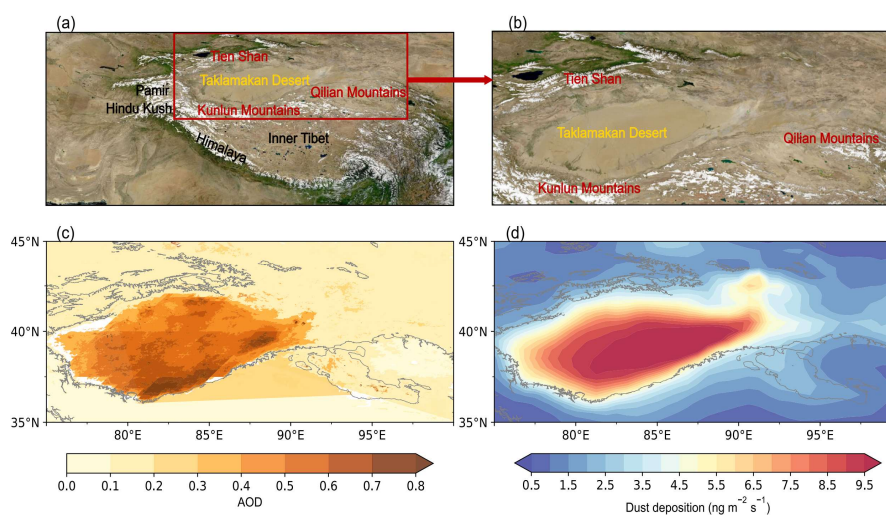
## 274 **3 Results**

### 275 **3.1 Remote sensing of the snow darkening effect across the high mountains** 276 **surrounding the TD**

277 The TD is located in the northern part of HMA and is surrounded by some of the highest  
278 mountain ranges on Earth, including the Kunlun Mountains, Tien Shan, and Pamir  
279 (Figures 2a and b). The TD region emits vast amounts of dust particles into the  
280 atmosphere each year, particularly during the spring and summer (Wang et al., 2008;  
281 Chen et al., 2013, 2017b; Kang et al., 2016; Wu et al., 2021; Tang et al., 2022); this  
282 phenomenon is confirmed by the high AOD levels at 550 nm from March to August



283 (Figure 2c). A significant amount of this dust is ultimately redeposited across the Tarim  
284 Basin and the surrounding mountains. The Tien Shan and Kunlun Mountains are two  
285 regions that experience high levels of dust deposition owing to the local topography  
286 and atmospheric circulation patterns (Figure 2d) (Huang et al., 2007, 2014; Ge et al.,  
287 2014; Dong et al., 2022). Therefore, we selected two typical cases to demonstrate the  
288 snow-darkening effect across the mountains surrounding the TD, a springtime dust  
289 event across the Tien Shan and a summertime dust event across the Kunlun Mountains.



290

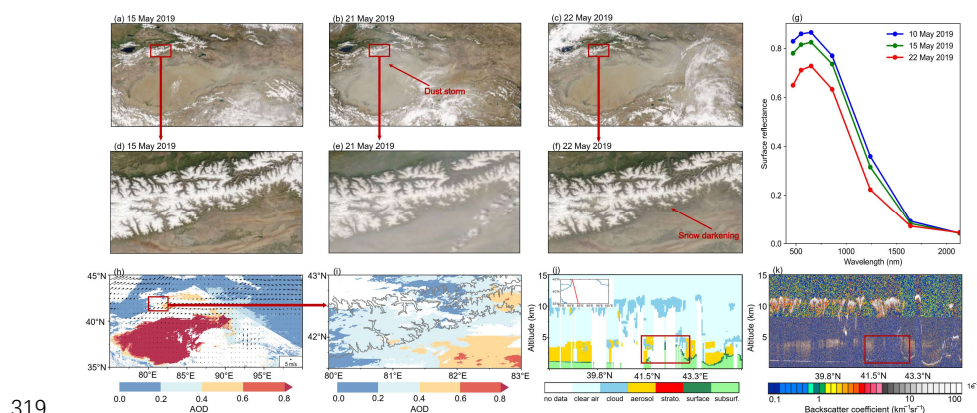
291 **Figure 2. Mountain ranges surrounding the Taklamakan Desert, and AOD and**  
292 **dust deposition distributions across the Taklamakan Desert and surrounding**  
293 **region. (a, b) Geographic location of the Taklamakan Desert and surrounding**  
294 **mountains. The red box defines the area in (b). Spatial distributions of the**  
295 **averaged (c) AOD and (d) dust deposition values, which were derived from**  
296 **MCD19A2 and MERRA-2 during the March to August 2019 period.**

### 297 **3.1.1 Dust-induced snow darkening across the Tien Shan**

298 A significant dust storm occurred across the TD region on 18–22 May 2019. The 21  
299 May 2019 Terra/MODIS satellite image (Figure 3b) showed that the dust plumes had  
300 spread to the north and east owing to an upper anticyclone system in the Tarim Basin  
301 (Figure 3h). Some dust particles were uplifted to >4 km altitude, as shown in the



302 CALIPSO aerosol vertical profiles (Figures 3j and k). These dust particles were then  
 303 transported to the snow-covered high-elevation areas of the Tien Shan, as illustrated in  
 304 the MODIS AOD images (Figures 3h and i). Dust plumes were also observed in a  
 305 satellite image that spanned the broadly snow-covered central Tien Shan (Figure 3e),  
 306 and the snow appeared to darken in the 22 May 2019 Terra/MODIS satellite image that  
 307 was acquired under the first clear-sky conditions after this severe dust event. However,  
 308 the snow was much whiter prior to the passage of this dust storm, as shown in Figures  
 309 3d and f. Figure 3g further illustrates changes in the surface reflectance of the snow-  
 310 covered areas, providing a more intuitive influence of dust deposition on the snow  
 311 physical properties. The reflectance was around 0.8 in the VIS spectrum on 15 May  
 312 2019, but quickly decreased to  $<0.7$  on 22 May 2019, after the passage of the dust  
 313 plumes. The reduction in VIS wavelengths was up to  $>0.1$  during this short time interval.  
 314 These observations show that the dust plumes from the TD can significantly darken the  
 315 snowpack across the Tien Shan through heavy dust deposition. Furthermore, the  
 316 progression of air-temperature-induced snow aging cannot effectively explain this  
 317 phenomenon. This result is consistent with previous satellite observations over the  
 318 Himalayas (Gautam et al., 2013).



320 **Figure 3. Satellite observations during the 18–22 May 2019 severe dust event**  
 321 **across the Tien Shan. (a, d) Terra/MODIS satellite true-color images acquired on**  
 322 **15 May 2019, prior to the dust storm. (b, e) Terra/MODIS satellite images**  
 323 **acquired on 21 May 2019, with the dust storm transport from the TD to the Tien**



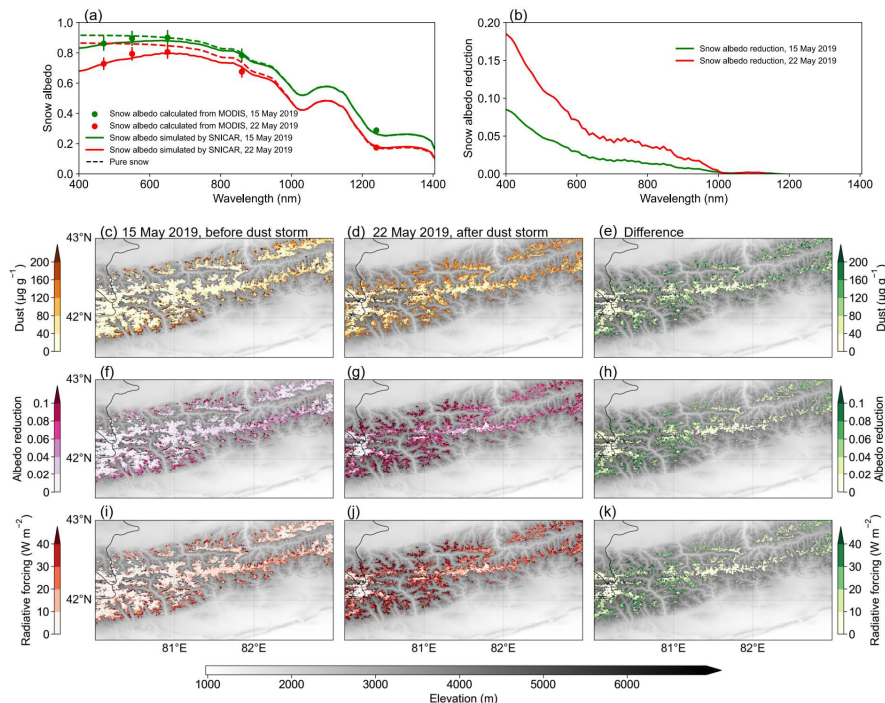
324 **Shan indicated by the red arrow in (b). (c, f) Terra/MODIS satellite images**  
325 **acquired on 22 May 2019, with significant snow darkening observed across the**  
326 **Tien Shan after the dust storm. (g) MOD09GA spectral surface reflectance across**  
327 **snow-covered areas on 10 May 2019 (blue), 15 May 2019 (green), and 22 May 2019**  
328 **(red). (h) MODIS AOD image on 21 May 2019, with the ERA5 daily mean wind**  
329 **vector at 700 hPa overlain. (i) MODIS AOD image across the Tien Shan on 21**  
330 **May 2019. Gray lines denote the 3000 m elevation contour. CALIPSO (j) vertical**  
331 **feature mask and (k) backscatter coefficient on 21 May 2019.**

332 We also derived the spectral snow albedo and retrieved several parameters to  
333 quantitatively assess the impact of this dust deposition on snow darkening. The  
334 SNICAR-simulated spectral snow albedo (solid lines) and MODIS-derived 5-band  
335 snow albedo (dots) in Figure 4a are averaged over the area in Figure 4c. These results  
336 demonstrate an agreement of >95%, thereby indicating the reliability of our retrievals.  
337 The spectral snow albedo reduction on 15 and 22 May 2019 are shown in Figure 4b.  
338 There were significant increases in the albedo reductions as the wavelength decreased,  
339 particularly on 22 May 2019, which is consistent with theoretical simulations of the  
340 dust-induced snow darkening effect (Figure 1). However, the spectral curve differed  
341 from the BC-induced results in the anthropogenically influenced areas of Northeast  
342 China (Wang et al., 2017; Niu et al., 2022) and Northwest China (Shi et al., 2020).  
343 Therefore, we indicate that the observed snow darkening in this study was mainly  
344 caused by natural dust emissions, as opposed to BC and organic carbon (OC) emissions  
345 from anthropogenic activities and/or biomass burning. There was a spectral snow  
346 albedo reduction of 0.02–0.08 in the VIS on 15 May 2019, which represents persistent  
347 but relatively low dust deposition during spring. However, the severe dust event caused  
348 a rapid increase in spectral snow albedo reduction to 0.045–0.18 in a matter of days.  
349 The approximate doubling of the albedo reduction indicates that the increase in the dust  
350 concentration was much greater than 100% based on the nonlinear theory of the snow  
351 albedo feedback to the dust concentration (Figure 1). This implies that it is important  
352 to consider both the frequency and intensity of dust events when examining their impact





353 on snow albedo. Similar phenomena that were induced by catastrophic wildfire events  
354 have been observed in the snowpack across New Zealand (Pu et al., 2021). These results  
355 suggest that extreme events may reflect the more pronounced impact of climate  
356 warming on our planet (Liang et al., 2021; Gui et al., 2022). Therefore, it is important  
357 to pay more attention to extreme events, rather than just conducting either annual or  
358 monthly averaged analyses, to fully capture the influence of climate change on snow  
359 albedo.



360  
361 **Figure 4.** (a) Averaged SNICAR-simulated spectral snow albedo (solid lines) and  
362 MODIS-derived 5-band snow albedo (dots) for the region across the Tien Shan  
363 impacted by the 18–22 May 2019 severe dust event. (b) Snow albedo reduction on  
364 15 May 2019 (green) and 22 May 2019 (red). Spatial distributions of the average  
365 (c, d) dust, (f, g) albedo reduction, and (i, j) radiative forcing on 15 and 22 May  
366 2019, respectively. Spatial distributions of the differences in (e) dust, (h) albedo  
367 reduction, and (k) radiative forcing between 15 and 22 May 2019. The background  
368 image in (c–k) is a grayscale topographic map of the Tien Shan.



369 Figures 4c and d illustrate the spatial distributions of the dust concentration in the  
370 snowpack on 15 and 22 May 2019, respectively. There was a sharp increase in the dust  
371 content from 2–55 to 42–192  $\mu\text{g g}^{-1}$  ( $\sim 2.67$ -fold increase) following the severe dust  
372 event, with the lower elevations possessing higher dust concentrations and greater dust  
373 content increases (Figures 4d and e). Snow darkening was observed across all of the  
374 snow-covered areas ( $>2100 \text{ km}^2$ ), including the summits, thereby highlighting the  
375 extensive influence of this severe dust event across the central Tien Shan. Furthermore,  
376 these results demonstrate the capability and effectiveness of employing satellite remote  
377 sensing to observe/monitor large-scale snow darkening. The dust-induced broadband  
378 snow albedo reductions and radiative forcing are shown in Figures 4f–k, with observed  
379 spatial patterns that are largely similar to the dust content distributions. The snow  
380 albedo reduction increased by 0.008–0.052, with an observed increase from 0.002–  
381 0.032 on 15 May to 0.028–0.079 on 22 May. The radiative forcing increased by 2.5–  
382 20.5  $\text{W m}^{-2}$ , with an observed increase from 0.5–12.5  $\text{W m}^{-2}$  on 15 May to 11–31.5  $\text{W}$   
383  $\text{m}^{-2}$  on 22 May (Figure S7). Both the snow albedo reduction and radiative forcing  
384 increased by a factor of  $\sim 2.39$ , which directly reflects its significant impact on the  
385 regional radiation balance and climate (Dumont et al., 2020). Snow darkening can also  
386 accelerate snow aging by absorbing more shortwave radiation in a warming spring, as  
387 characterized by the  $R_{\text{eff}}$  growth (Figures S3a–c).

### 388 **3.1.2 Dust-induced snow darkening across the Kunlun Mountains**

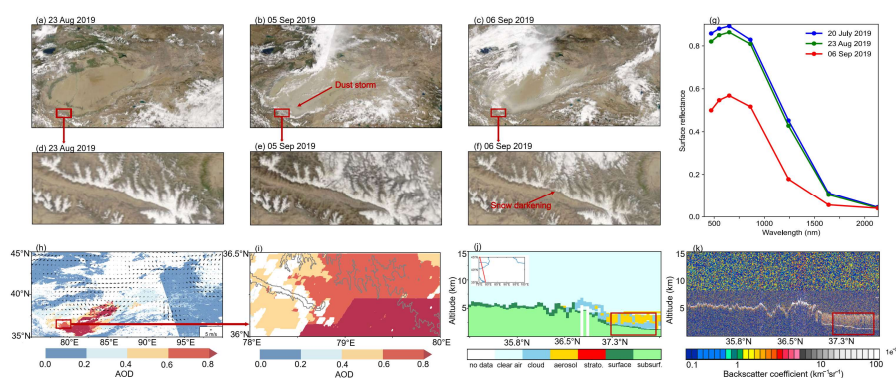
389 The Kunlun Mountains are located along the southern (northern) edge of the Tarim  
390 Basin (Tibetan Plateau). The northern slope of the Central/West Kunlun Mountains  
391 directly faces the TD (Figure 1a) and should have experienced the most severe dust-  
392 induced snow darkening. Similar conditions also exist across the Himalayas, where the  
393 south slope faces both the Thar Desert in India and the Middle East. We captured a  
394 typical dust storm event with associated dust deposition and snow darkening that  
395 occurred between 5 and 11 May 2020 along the northern slope of the Kunlun Mountains  
396 using MODIS satellite images (Figure S2). The previously mentioned spring  
397 phenomenon is well-known due to intense springtime dust emissions from the TD,





398 whereas the summer phenomenon is usually overlooked. However, it has been shown  
399 that dust can more effectively cross the Kunlun Mountains during the summer months,  
400 with the potential to induce changes in atmospheric dynamics and thermal effects (Yuan  
401 et al., 2018). Therefore, we specifically chose a summer case to highlight snow  
402 darkening across the Kunlun Mountains.

403



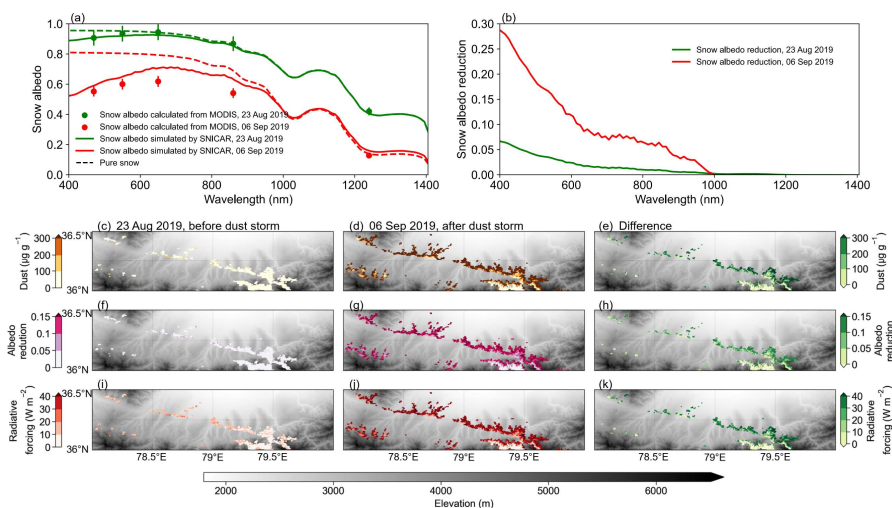
404

405 **Figure 5. Satellite observations during the 26 Aug to 08 Sep 2019 dust storm across**  
406 **the Kunlun Mountains. (a, d) Terra/MODIS satellite true-color images acquired**  
407 **on 23 Aug 2019, prior to the dust storm. (b, e) Terra/MODIS satellite images**  
408 **acquired on 05 Sep 2019, with the dust storm transport from the TD to the Kunlun**  
409 **Mountains indicated by the red arrow in (b). (c, f) Terra/MODIS satellite images**  
410 **acquired on 06 Sep 2019, with significant snow darkening across the Kunlun**  
411 **Mountains after the dust storm. (g) MOD09GA spectral surface reflectance over**  
412 **the snow-covered areas on 20 July 2019 (blue), 23 Aug 2019 (green), and 06 Sep**  
413 **2019 (red). (h) MODIS AOD image on 05 Sep 2019, with the ERA5 daily mean**  
414 **wind vector at 700 hPa overlain. (i) MODIS AOD image across the Kunlun**  
415 **Mountains on 05 Sep 2019. Gray lines denote the 3000-m elevation contour.**  
416 **CALIPSO (j) vertical feature mask and (k) backscatter coefficient on 04 Sep 2019.**

417 A significant dust event that impacted the northern slope of the Kunlun Mountains  
418 occurred from 26 Aug to 08 Sep 2019 (Figure 5b). The Terra/MODIS satellite images  
419 on 5 Sep 2019 (Figures 5b and e) show the accumulation of dust plumes along the



420 southern edge of the Tarim Basin. In summer, the westerlies weaken and shift to the  
 421 north, leading to more accumulation of dust locally instead of transporting it eastward  
 422 (Chen et al., 2017a; Yuan et al., 2018). Furthermore, the enhanced sensible heat flux  
 423 favors the southward transport of uplifted dust, leading to cyclonic convergence at the  
 424 surface and anticyclonic divergence at the top of the troposphere above the TD (Figure  
 425 5h). The synergistic effects of atmospheric dynamic and thermal forcing can cause the  
 426 dust plumes to be uplifted to ~5 km altitude (Figures 5j–k). This uplift effectively  
 427 facilitated the dust plume ascent to the snow-covered areas across the northern slope of  
 428 the Kunlun Mountains (Figure 5e and i). A comparison of the MODIS images that were  
 429 acquired on 23 Aug and 6 Sep 2019 highlighted snow darkening after this severe dust  
 430 storm (Figures 5d and f). The surface reflectance decreased by ~0.22 in the VIS  
 431 spectrum, decreasing from 0.285 on 23 Aug to ~0.065 on 5 Sep. These observations  
 432 indicate that this summertime dust event caused significant snow darkening across the  
 433 Kunlun Mountains.



434  
 435 **Figure 6. (a) Averaged SNICAR-simulated spectral snow albedo (solid lines) and**  
 436 **MODIS-derived 5-band snow albedo (dots) for the region across the Kunlun**  
 437 **Mountains impacted by the 26 Aug to 08 Sep 2019 severe dust event. (b) Snow**  
 438 **albedo reductions on 23 Aug 2019 (green) and 06 Sep 2019 (red). Spatial**  
 439 **distributions of the average (c, d) dust, (f, g) albedo reduction, and (i, j) radiative**  
 440 **forcing on 23 Aug and 06 Sep 2019, respectively. Spatial distributions of the**



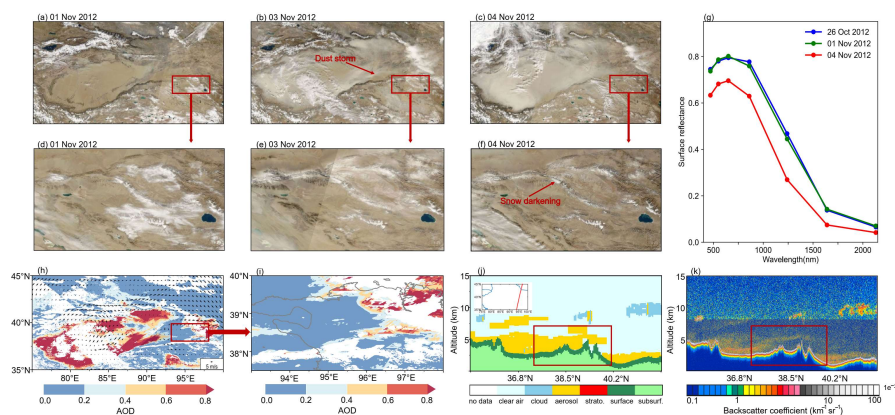
441 **differences in (e) dust, (h) albedo reduction, and (k) radiative forcing between 23**  
442 **Aug and 06 Sep 2019. The background image in (c–k) is a grayscale topographic**  
443 **map of the Kunlun Mountains.**

444 Figure 6 provides a more quantitative investigation of the impact of this severe dust  
445 event on the snowpack across the Kunlun Mountains, whereby a significant increase in  
446 dust content from 12–50  $\mu\text{g g}^{-1}$  on 23 Aug to 170–360  $\mu\text{g g}^{-1}$  on 06 Sep (~6.45-fold  
447 increase) is observed after this severe dust event. The darkened snow-covered area  
448 spans  $>600 \text{ km}^2$ , with a clear south–north gradient in the dust concentration distribution  
449 that is influenced by both the orientation and elevation of the mountains. This large dust  
450 deposition induced a 0.015–0.106 increase in snow albedo reduction, with an observed  
451 increase from 0.013–0.032 on 23 Aug to 0.088–0.136 on 06 Sep. There was also a  
452 substantial increase in radiative forcing of 4.1–37.5  $\text{W m}^{-2}$ , with an observed increase  
453 from 3–11  $\text{W m}^{-2}$  on 23 Aug to 31–49  $\text{W m}^{-2}$  on 06 Sep (Figure S7). Note that these  
454 increases in both the snow albedo reduction and radiative forcing are approximately  
455 two times larger than those observed over the Tien Shan. These findings indicate  
456 accelerated snow aging, as evidenced by the faster growth rate of the  $R_{\text{eff}}$  observed  
457 across the Kunlun Mountains (Figures S4 and S5).

### 458 **3.1.3 Snow darkening across the Qilian Mountains**

459 Unlike the Tien Shan and Kunlun Mountains, the Qilian Mountains are located  
460 approximately 1000 km east of the Tarim Basin. The Hexi Corridor, a narrow and  
461 relatively flat plain that lies between the high-elevation, inhospitable terrains of the  
462 Mongolian and Tibetan plateaus (see Figure 2), is situated to the north of the Qilian  
463 Mountains. The unique terrain of the region results in TD dust plumes following a  
464 preferred transport route across the Hexi Corridor to East Asia (Zhang et al., 2008;  
465 Meng et al., 2018). These dust plumes are generally uplifted to  $>4 \text{ km}$  altitude and  
466 entrained in the westerlies (Huang et al., 2008; Dong et al., 2014; Chen et al., 2022),  
467 thereby providing a means for dust deposition onto the snowpack across the Qilian  
468 Mountains.

469



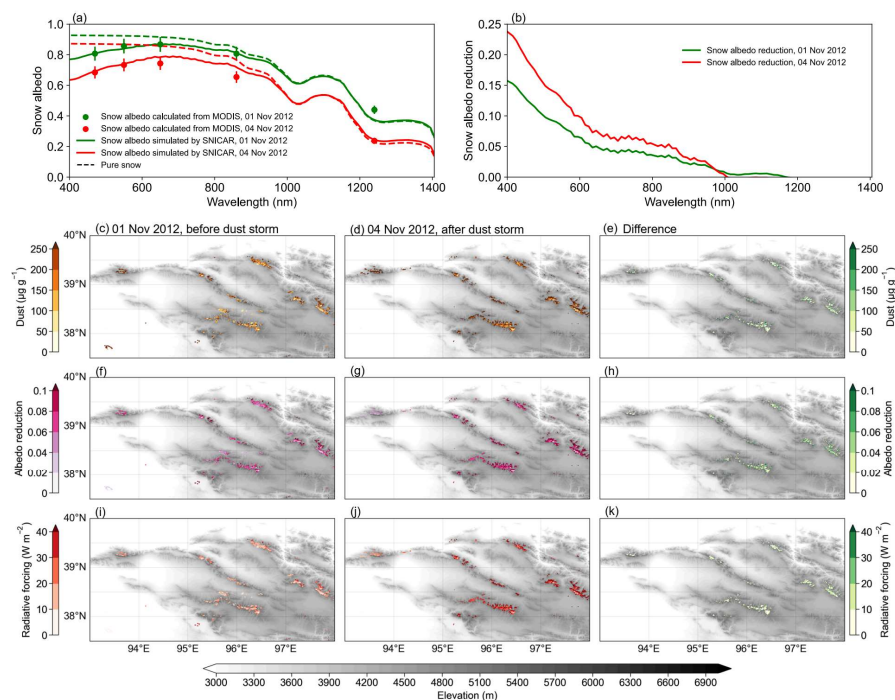
470

471 **Figure 7. Satellite observations during the 02–04 Nov 2012 dust storm across the**  
472 **Qilian Mountains. (a, d) Terra/MODIS satellite true-color images acquired on 01**  
473 **Nov 2012, prior to the dust storm. (b, e) Terra/MODIS satellite images acquired**  
474 **on 03 Nov 2012, with the dust transport from the TD to the Qilian Mountains**  
475 **indicated by the red arrow in (b). (c, f) Terra/MODIS satellite images acquired on**  
476 **04 Nov 2012, with significant snow darkening observed across the Qilian**  
477 **Mountains after the dust storm. (g) MOD09GA spectral surface reflectance over**  
478 **the snow-covered areas on 26 Oct 2012 (blue), 01 Nov 2012 (green), and 04 Nov**  
479 **2012 (red). (h) MODIS AOD image on 03 Nov 2012, with the ERA5 daily mean**  
480 **wind vector at 700 hPa overlain. (i) MODIS AOD image across the Qilian**  
481 **Mountains on 03 Nov 2012. The gray line denotes the 3000-m elevation contour.**  
482 **CALIPSO (j) vertical feature mask and (k) backscatter coefficient on 03 Nov 2012.**

483 Figure 7 illustrates a severe dust event that occurred from 02 to 04 Nov 2012, when  
484 abundant dust plumes were being transported across the narrow Hexi Corridor (Figures  
485 7b and h). The dust content was much more intense in this region, possessing AOD  
486 levels of up to  $>0.8$ . Furthermore, the CALIPSO observations indicated that the dust  
487 plumes were uplifted to  $\sim 10$  km altitude (Figures 7j and k), thereby allowing some dust  
488 particles to cross over the northern slopes of the Qilian Mountains and spread across its  
489 western extent (Figures 7e and i). The average reflectance in the VIS spectrum was  
490 stable at around 0.7–0.8 across the snow-covered areas about a week before the severe



491 dust event but then significantly decreased to 0.6–0.7 owing to heavy dust deposition



492

493 **Figure 8. (a) Averaged SNICAR-simulated spectral snow albedo (solid lines) and**  
 494 **MODIS-derived 5-band snow albedo (dots) for the region across the Qilian**  
 495 **Mountains impacted by the 02–04 Nov 2012 severe dust event. (b) Snow albedo**  
 496 **reductions on 01 Nov 2012 (green) and 04 Nov 2012 (red). Spatial distributions of**  
 497 **the average (c, d) dust, (f, g) albedo reduction, and (i, j) radiative forcing on 01**  
 498 **and 04 Nov 2012, respectively. Spatial distributions of the differences in (e) dust,**  
 499 **(h) albedo reduction, and (k) radiative forcing between 01 and 04 Nov 2012. The**  
 500 **background image in (c–k) is a grayscale image of the Qilian Mountains.**

501 Figure 8 presents the quantitative satellite-derived results, which highlight a rapid  
 502 increase in dust content from 110–228 to 194–360  $\mu\text{g g}^{-1}$  (~1.53-fold increase) that  
 503 spanned a snow-covered area of  $>630 \text{ km}^2$  (Figures 8f–h). This significant increase in  
 504 dust content led to a considerable increase in snow albedo reduction (radiative forcing)  
 505 of 0.018–0.067 (3–16  $\text{W m}^{-2}$ ), which increased from 0.042–0.076 (11–20  $\text{W m}^{-2}$ ) on 1

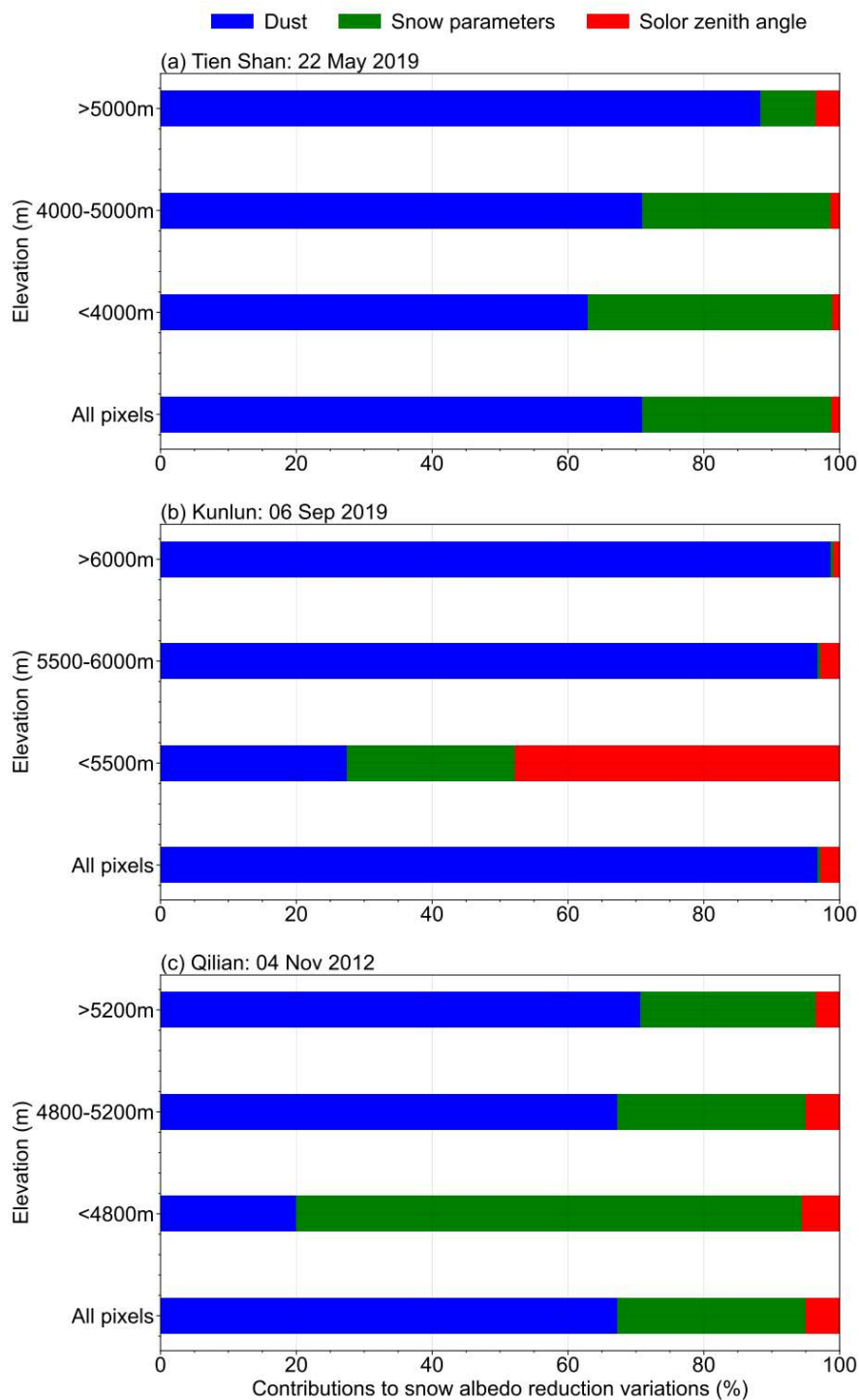


506 Nov 2012 to  $0.092-0.153$  ( $22-38 \text{ W m}^{-2}$ ) on 4 Nov 2012 (Figure S7). This >1.5-fold  
507 increase in snow albedo reduction (radiative forcing) was not solely due to the  
508 deposition of dust. Accelerated snow aging, which was observed from the enhanced  
509  $R_{\text{eff}}$  growth (Figure S6), also contributed to the observed increase in snow albedo  
510 reduction (radiative forcing); this trend was similar to that observed across the Kunlun  
511 Mountains. Our approach uses satellite remote sensing to obtain a more complete  
512 spatiotemporal evolution of the TD dust storm, including its emission, long-range  
513 transport, and deposition, across the Qilian Mountains, which offers advantages over  
514 previous field measurements (Wei et al., 2017).

### 515 **3.2 Contributions to the spatial and altitudinal variations in dust-induced snow** 516 **darkening**

517 We quantified the contributions of the three key factors (dust content, snow properties,  
518 and solar zenith) to the spatial variations in snow albedo reduction (Figure 9) using the  
519 method described in Section 2.6. The dust content was the dominant contributor to the  
520 spatial variations in snow darkening. This is at least partially attributed to the greater  
521 spatial differences in dust content compared with those of the other factors, as shown  
522 in Figures 4, 6, and 8. Furthermore, theoretical modeling has indicated that the snow  
523 albedo reduction is more sensitive to changes in dust content than to changes in the  
524 snow properties and solar zenith angle (Flanner et al., 2021; Usha et al., 2022; Zhao et  
525 al., 2022). Laboratory experiments also support these findings (Zhang et al., 2018; Li  
526 et al., 2022). The contribution of the dust content also increased as the elevation in each  
527 mountain range increased, whereas a decreasing trend was observed for the snow  
528 parameters. This is because the dust content exhibits spatial differences across all of the  
529 elevations owing to its widespread and heterogeneous depositions. However, the snow  
530 depth has a more semi-infinite nature and  $R_{\text{eff}}$  exhibits greater spatial homogeneity at  
531 higher elevations owing to slower snow aging.



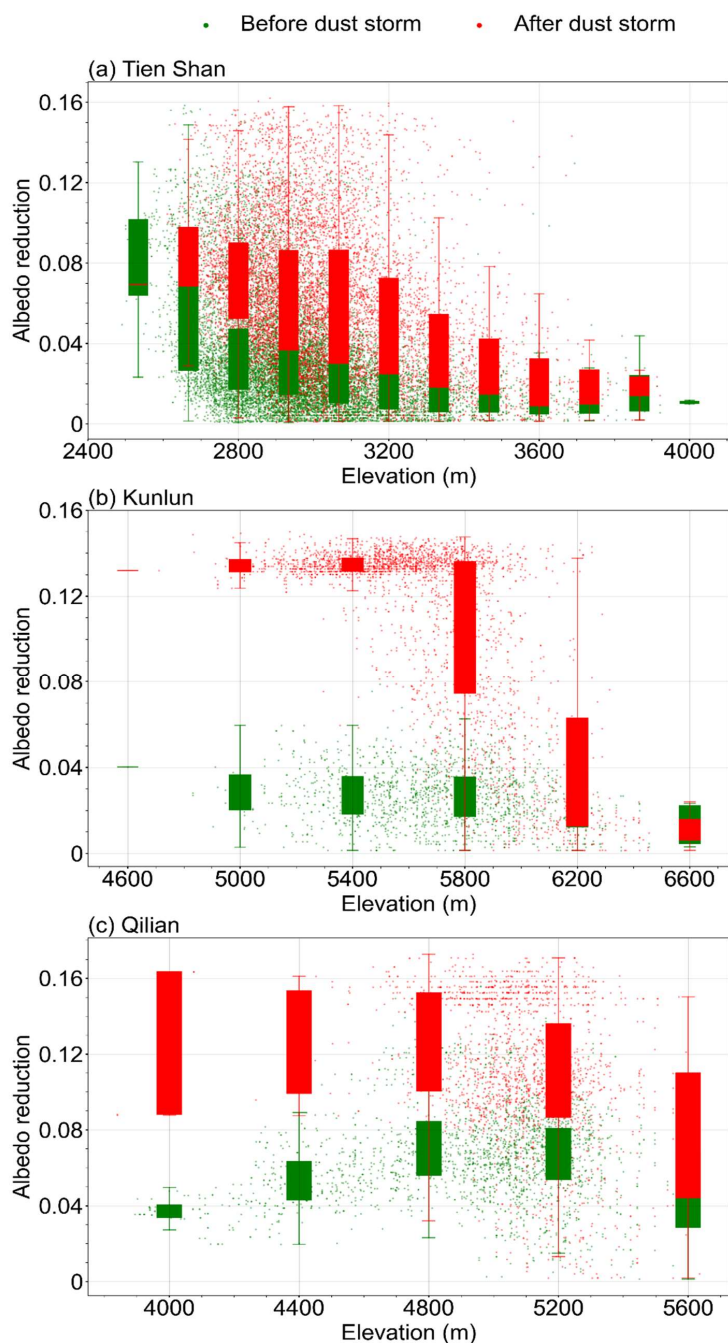




533 **Figure 9. Contributions of the spatial variations in dust content (blue), snow**  
534 **parameters (green), and solar zenith angle (red) to the snow albedo reduction at**  
535 **different elevations across the (a) Tien Shan, (b) Kunlun Mountains, and (c) Qilian**  
536 **Mountains.**

537 Scatter plots of the snow albedo reduction for the elevations across the Tien Shan,  
538 Kunlun Mountains, and Qilian Mountains are shown in Figure 10. The snow albedo  
539 reduction across the Tien Shan decreased with increasing elevation prior to the dust  
540 storm. However, the most severe dust deposition occurred within the 4000–4500 m  
541 elevation range, resulting in the most significant enhancement of snow albedo reduction  
542 in this elevation range. These findings are consistent with those reported for the  
543 Himalayas (Sarangi et al., 2020). The snow albedo reduction was generally low across  
544 the Kunlun Mountains for all of the elevation ranges. However, dust deposition caused  
545 the most significant albedo reduction within the 4500–5500 m elevation range, with a  
546 dramatic decrease of its influence above 6000 m. These findings correspond to the  
547 CALIPSO aerosol vertical profile observations (Figures 5j and k). The snow albedo  
548 reduction across the Qilian Mountains initially increased with elevation up to ~5000 m  
549 and then decreased at high elevations prior to the dust storm. However, the most severe  
550 dust deposition occurred across the lower elevations, leading to the most significant  
551 enhancement of snow albedo reduction across these lower-elevation regions. Our  
552 elevation analysis revealed a consistent outcome, whereby the dust storms significantly  
553 darkened the snowpack up to >5000 m elevation across the three analyzed mountain  
554 ranges.





555

556 **Figure 10. Scatter plots of the snow albedo reductions for the analyzed elevation**  
557 **ranges across the (a) Tien Shan, (b) Kunlun Mountains, and (c) Qilian Mountains.**

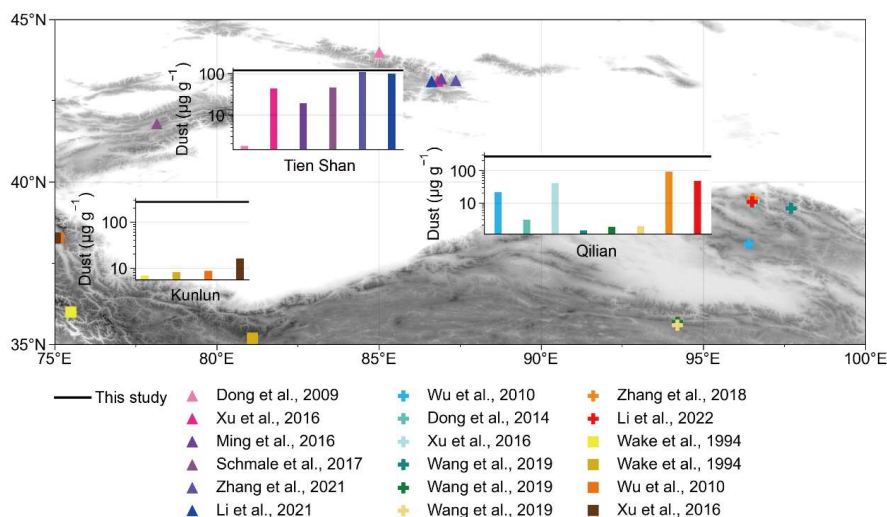
558 **Each box plot shows the statistical results for a 400-m elevation interval.**



559 **4 Discussion**

560 The snow darkening effect and its resultant radiative forcing have gained increasing  
561 attention in recent decades owing to their significant impacts on regional climate and  
562 hydrological systems. However, studies in the Tien Shan, Kunlun Mountains, and  
563 Qilian Mountains have been limited to local-scale observations, despite the significant  
564 impact of dust on snow darkening in these regions. Here we provide an overview of  
565 previous in situ dust-content measurements in the snowpack across the study region for  
566 comparison with our satellite remote-sensing results (see Figure 11). In the Tien Shan  
567 region, Ming et al. (2016), Xu et al. (2016), Li et al. (2021), and Zhang et al. (2021)  
568 reported a dust content of 19.3–110  $\mu\text{g g}^{-1}$  in the snowpack across Urumqi Glacier No.1.  
569 Dong et al. (2009) observed an average dust content of 0.97–3.69  $\mu\text{g g}^{-1}$  in the  
570 snowpack across Urumqi Glacier No. 1, Haxilegen Glacier No. 51, and Miaoergou  
571 Glacier. Schmale et al. (2017) found a variable dust content of 68.1–125.9  $\mu\text{g g}^{-1}$  in the  
572 snowpack across Suez Zapadny, No. 354, and Golubin glaciers in the western Tien  
573 Shan. In the Kunlun Mountains, Wake et al. (1994) reported a dust content of up to  $\sim 8$   
574  $\mu\text{g g}^{-1}$  in the snow/ice across the western Kunlun Mountains. Wu et al. (2010) and Xu  
575 et al. (2016) measured dust contents of  $\sim 8.68$  and 16.24  $\mu\text{g g}^{-1}$  in the ice core and  
576 snowpack across Muztagata Glacier in the northwestern Tibet Plateau (Wu et al., 2010;  
577 Xu et al., 2016), respectively. In the Qilian Mountains, Wu et al. (2010) analyzed ice  
578 cores from Dunde Glacier and measured a dust content of  $\sim 21$   $\mu\text{g g}^{-1}$ . The measured  
579 dust contents in the snowpack across Laohugou Glacier ranged from around 3 to 93.2  
580  $\mu\text{g g}^{-1}$  (Dong et al., 2014; Xu et al., 2016; Zhang et al., 2018; Li et al., 2022). Wang et  
581 al. (2019) measured a variable dust content of 1.4–1.9  $\mu\text{g g}^{-1}$  in the fresh snow across  
582 Qiyi, Meikuang, and Yuzhufeng glaciers. Overall, previous field studies have reported  
583 dust contents of 0.97–125.9, 6.78–16.24, and 1.4–93.2  $\mu\text{g g}^{-1}$  for the Tien Shan, Kunlun  
584 Mountains, and Qilian Mountains, respectively.

585



586

587

588

589

**Figure 11. Comparisons of the satellite-derived dust contents (black lines) in snow from this study and observed values from previous studies (colored symbols and bars).**

590

591

592

593

594

595

596

597

598

599

600

601

602

603

604

605

Our satellite-derived approach has yielded much higher dust contents than those obtained via in situ field measurements, with 42–196, 170–360, and 194–360  $\mu\text{g g}^{-1}$  determined for the Tien Shan, Kunlun Mountains, and Qilian Mountains, respectively. A key reason for this discrepancy could be that the field measurements usually record the background dust content signal, which includes a gradual natural deposition of dust, whereas our analysis specifically focused on significant snow darkening events due to severe dust storms, which further highlights the advantage of employing remote-sensing techniques to observe extreme snow darkening phenomena. We do note that satellite-derived approaches possess their own uncertainties, which arise from the data resolution and accuracy, algorithm assumptions, and atmospheric and underlying surface interferences (Cui et al., 2021). Nevertheless, this satellite-derived approach remains a valuable tool for effectively and rapidly studying extreme events, which cannot be captured by field measurements or climate model simulations, particularly as these extreme events will become increasingly important for climate and hydrological systems as the global climate continues to warm (Clow et al., 2016; Dumont et al., 2020).



606 Given the significant snow darkening effect highlighted in this study and recent  
607 observations of decreasing snow cover across the Tien Shan, Kunlun Mountains, and  
608 Qilian Mountains (She et al., 2015; Li et al., 2020; Zhu et al., 2022), it is crucial to  
609 evaluate the impact of snow darkening on regional hydrologic cycles and local  
610 freshwater supplies. However, snow aging and melting mechanisms are complex and  
611 therefore require complementary observations because remote sensing alone cannot  
612 distinguish the influences of augmented shortwave radiation owing to dust and  
613 increased air temperatures on snow aging and melting (Gautam et al., 2013). Additional  
614 research that integrates model simulations and satellite observations is necessary to  
615 differentiate the roles of snow darkening and global warming in enhancing snow aging  
616 and melting, and the resultant changes in glacier runoff in the future.

## 617 **5 Conclusions**

618 The Taklamakan Desert, the second-largest shifting sand desert on Earth, annually  
619 emits vast amounts of dust into the atmosphere that eventually settles onto the  
620 snowpack across the surrounding high mountains. We combined MODIS satellite data  
621 analysis and SNICAR model simulations to reveal significant snow-darkening events  
622 and quantify the snow albedo reduction and radiative forcing caused by severe dust  
623 storms.

624 The satellite observations captured significant snow darkening over the 3000–6000 m  
625 elevation range across the Tien Shan and Kunlun Mountains, which could be attributed  
626 to the high uplift of dust owing to the local topography and atmospheric circulation.  
627 The impacted area spanned the track of the dust storm and impacted almost all of the  
628 snow-covered areas across the Tien Shan ( $>2100 \text{ km}^2$ ) and Kunlun Mountains ( $>600$   
629  $\text{km}^2$ ), including the summits. The dust content in the snowpack increased to 42–192  
630 and 170–360  $\mu\text{g g}^{-1}$ , with significant increases in snow albedo reduction (radiative  
631 forcing) of 0.028–0.079 ( $11\text{--}31.5 \text{ W m}^{-2}$ ) and 0.088–0.136 ( $31\text{--}49 \text{ W m}^{-2}$ ) across the  
632 Tien Shan and Kunlun Mountains, respectively. Furthermore, these dust events  
633 accelerated snow aging, as indicated by the  $R_{\text{eff}}$  growth. The dust plumes from the  
634 Taklamakan Desert also traveled to the east, almost 1000 km from the Tarim Basin,



635 and deposited dust across much of the snow-covered area ( $>630 \text{ km}^2$ ) in the Qilian  
636 Mountains. This dust deposition significantly increased the dust content to  $194\text{--}360 \mu\text{g}$   
637  $\text{g}^{-1}$ , causing a considerable increase in snow albedo reduction (radiative forcing) of  
638  $0.092\text{--}0.153$  ( $22\text{--}38 \text{ W m}^{-2}$ ). The spatial distribution of the snow-darkening effect  
639 varied across all three mountain ranges owing to the uneven deposition of dust.  
640 Furthermore, the most significant snow darkening was observed in the high elevation  
641 range ( $4000\text{--}5500 \text{ m}$ ). We also compared our satellite-derived results with previous  
642 field measurements. Our results indicate that severe dust storms, which occur over short  
643 periods, have a more profound effect on snow darkening compared with the relatively  
644 slow deposition of dust when there are no dust storms. We therefore demonstrate that  
645 satellite-derived analyses of dust deposition and its impact on snow albedo and radiative  
646 forcing are crucial for rapidly and accurately capturing extreme dust deposition events  
647 that may be difficult to detect through field measurements and climate model  
648 simulations.

649

650

651

652

653

654

655

656

657

658

659



660 *Data availability.* All datasets and codes used to produce this study can be obtained by  
661 contacting Wei Pu ([puwei@lzu.edu.cn](mailto:puwei@lzu.edu.cn)).

662 *Author contributions.* WP and XW designed the study and developed the overarching  
663 research goals and aims. YX carried the study out and wrote the first draft with  
664 contributions from all co-authors. YX processed the data with the assistance of YC, SY,  
665 TS, XC, XN, DW and JC. WP and XW assumed oversight and leadership responsibility  
666 for the research activity planning and execution. All authors contributed to the  
667 improvement of results and revised the final paper.

668 *Competing interests.* The authors declare that they have no conflict of interest.

669 *Acknowledgements.* The Lanzhou University group acknowledges support from the  
670 National Science Fund for Distinguished Young Scholars, the State Key Laboratory of  
671 Cryosphere Science Open Fund and the National Natural Science Foundation of China.  
672 We appreciate Dr. Boyuan Zhang's assistance with the code improvements. We thank  
673 Lanzhou City's scientific research funding subsidy to Lanzhou University and the  
674 Supercomputing Center of Lanzhou University for providing the computing services.

675 *Financial support.* This research was supported by the National Science Fund for  
676 Distinguished Young Scholars (42025102), the State Key Laboratory of Cryosphere  
677 Science Open Fund (SKLCS-OP-2021-05) and the National Natural Science  
678 Foundation of China (42075061).



679 **Reference**

- 680 Bair, E. H., Stillinger, T., and Dozier, J.: Snow property inversion from remote sensing  
681 (SPIReS): A generalized multispectral unmixing approach with examples from  
682 MODIS and Landsat 8 OLI, *IEEE Transactions on Geoscience and Remote*  
683 *Sensing*, 59, 7270-7284, 10.1109/tgrs.2020.3040328, 2020.
- 684 Baladima, F., Thomas, J. L., Voisin, D., Dumont, M., Junquas, C., Kumar, R., Lavaysse,  
685 C., Marelle, L., Parrington, M., and Flemming, J.: Modeling an extreme dust  
686 deposition event to the French Alpine seasonal snowpack in April 2018:  
687 Meteorological context and predictions of dust deposition, *Journal of Geophysical*  
688 *Research: Atmospheres*, 127, 10.1029/2021jd035745, 2022.
- 689 Bormann, K. J., Brown, R. D., Derksen, C., Painter, T. H.: Estimating snow-cover  
690 trends from space, *Nature Climate Change*, 11, 924-928, 10.1038/s41558-018-  
691 0318-3, 2018.
- 692 Chen, B., Song, Z., Huang, J., Zhang, P., Hu, X., Zhang, X., Guan, X., Ge, J., and Zhou,  
693 X.: Estimation of atmospheric PM<sub>10</sub> Concentration in China using an  
694 interpretable deep learning model and top-of-the-atmosphere reflectance data from  
695 China's new generation geostationary meteorological satellite, FY-4A, *Journal of*  
696 *Geophysical Research: Atmospheres*, 127, 10.1029/2021jd036393, 2022.
- 697 Chen, S., Huang, J., Zhao, C., Qian, Y., Leung, L. R., and Yang, B.: Modeling the  
698 transport and radiative forcing of Taklimakan dust over the Tibetan Plateau: A case  
699 study in the summer of 2006, *Journal of Geophysical Research: Atmospheres*, 118,  
700 797-812, 10.1002/jgrd.50122, 2013.
- 701 Chen, S., Huang, J., Li, J., Jia, R., Jiang, N., Kang, L., Ma, X., and Xie, T.: Comparison  
702 of dust emissions, transport, and deposition between the Taklimakan Desert and  
703 Gobi Desert from 2007 to 2011, *Science China Earth Sciences*, 60, 1338-1355,  
704 10.1007/s11430-016-9051-0, 2017a.
- 705 Chen, S., Huang, J., Kang, L., Wang, H., Ma, X., He, Y., Yuan, T., Yang, B., Huang, Z.,  
706 and Zhang, G.: Emission, transport, and radiative effects of mineral dust from the  
707 Taklimakan and Gobi deserts: comparison of measurements and model results,  
708 *Atmospheric Chemistry and Physics*, 17, 2401-2421, 10.5194/acp-17-2401-2017,  
709 2017b.
- 710 Chen, W., Wang, X., Cui, J., Cao, X., Pu, W., Zheng, X., Ran, H., and Ding, J.: Radiative  
711 forcing of black carbon in seasonal snow of wintertime based on remote sensing  
712 over Xinjiang, China, *Atmospheric Environment*, 247,  
713 10.1016/j.atmosenv.2021.118204, 2021.
- 714 Clow, D. W., Williams, M. W., and Schuster, P. F.: Increasing aeolian dust deposition to  
715 snowpacks in the Rocky Mountains inferred from snowpack, wet deposition, and  
716 aerosol chemistry, *Atmospheric Environment*, 146, 183-194,  
717 10.1016/j.atmosenv.2016.06.076, 2016.
- 718 Cohen, J. and Rind, D.: The Effect of Snow Cover on the Climate, *J. Climate*, 4, 689-  
719 706, 10.1175/1520-0442(1991)004<0689:Teosco>2.0.Co;2, 1991.
- 720 Copernicus Climate Change Service: ERA5: Fifth generation of ECMWF atmospheric  
721 reanalysis of the global climate, Copernicus Climate Change Service Climate Data  
722 Store (CDS), 2017.





- 723 Cordero, R., Sepúlveda, E., Feron, S., Damiani, A., Fernandoy, F., Neshyba, S., Rowe,  
724 P. M., Asencio, V., Carrasco, J., Alfonso, J. A., Llanillo, P., Wachter, P., Seckmeyer,  
725 G., Stepanova, M., Carrera, J. M., Jorquera, J., Wang, C., Malhotra, A., Dana, J.,  
726 Khan, A. L., and Casassa, G.: Black carbon footprint of human presence in  
727 Antarctica, *Nature Communications*, 13, 2041-1723, s41467-022-28560-w, 2022.
- 728 Cui, J., Shi, T., Zhou, Y., Wu, D., Wang, X., and Pu, W.: Satellite-based radiative forcing  
729 by light-absorbing particles in snow across the Northern Hemisphere,  
730 *Atmospheric Chemistry and Physics*, 21, 269-288, 10.5194/acp-21-269-2021,  
731 2021.
- 732 Dang, C., Warren, S. G., Fu, Q., Doherty, S. J., Sturm, M., and Su, J.: Measurements of  
733 light-absorbing particles in snow across the Arctic, North America, and China:  
734 Effects on surface albedo, *Journal of Geophysical Research: Atmospheres*, 122,  
735 10.1002/2017jd027070, 2017.
- 736 Di Mauro, B., Fava, F., Ferrero, L., Garzonio, R., Baccolo, G., Delmonte, B., and  
737 Colombo, R.: Mineral dust impact on snow radiative properties in the European  
738 Alps combining ground, UAV, and satellite observations, *Journal of Geophysical  
739 Research: Atmospheres*, 120, 6080-6097, 10.1002/2015jd023287, 2015.
- 740 Dong, Z., Li, Z., Wang, F., and Zhang, M.: Characteristics of atmospheric dust  
741 deposition in snow on the glaciers of the eastern Tien Shan, China, *Journal of  
742 Glaciology*, 55, 797-804, 10.3189/002214309790152393, 2009.
- 743 Dong, Z., Qin, D., Chen, J., Qin, X., Ren, J., Cui, X., Du, Z., and Kang, S.:  
744 Physicochemical impacts of dust particles on alpine glacier meltwater at the  
745 Laohugou Glacier basin in western Qilian Mountains, China, *Science of the Total  
746 Environment*, 493, 930-942, 10.1016/j.scitotenv.2014.06.025, 2014.
- 747 Dong, Z., Brahney, J., Kang, S., Elser, J., Wei, T., Jiao, X., and Shao, Y.: Aeolian dust  
748 transport, cycle and influences in high-elevation cryosphere of the Tibetan Plateau  
749 region: New evidences from alpine snow and ice, *Earth-Science Reviews*, 211,  
750 10.1016/j.earscirev.2020.103408, 2020.
- 751 Dong, Q., Huang, Z., Li, W., Li, Z., Song, X., Liu, W., Wang, T., Bi, J., and Shi, J.:  
752 Polarization lidar measurements of dust optical properties at the junction of the  
753 Taklimakan Desert–Tibetan Plateau, *Remote Sensing*, 14, 10.3390/rs14030558,  
754 2022.
- 755 Dumont, M., Brun, E., Picard, G., Michou, M., Libois, Q., Petit, J. R., Geyer, M., Morin,  
756 S., and Josse, B.: Contribution of light-absorbing impurities in snow to  
757 Greenland's darkening since 2009, *Nature Geoscience*, 7, 509-512,  
758 10.1038/ngeo2180, 2014.
- 759 Dumont, M., Tuzet, F., Gascoin, S., Picard, G., Kutuzov, S., Lafaysse, M., Cluzet, B.,  
760 Nheili, R., and Painter, T. H.: Accelerated snow melt in the Russian Caucasus  
761 Mountains after the Saharan dust outbreak in March 2018, *Journal of Geophysical  
762 Research: Earth Surface*, 125, 10.1029/2020jf005641, 2020.
- 763 Flanner, M. G., Zender, C. S., Randerson, J. T., and Rasch, P. J.: Present-day climate  
764 forcing and response from black carbon in snow, *Journal of Geophysical Research*,  
765 112, 10.1029/2006jd008003, 2007.
- 766 Flanner, M. G., Zender, C. S., Hess, P. G., Mahowald, N. M., Painter, T. H., Ramanathan,





- 767 V., and Rasch, P. J.: Springtime warming and reduced snow cover from  
768 carbonaceous particles, *Atmospheric Chemistry and Physics*, 9, 2481–2497,  
769 10.5194/acp-9-2481-2009, 2009.
- 770 Flanner, M. G., Arnheim, J. B., Cook, J. M., Dang, C., He, C., Huang, X., Singh, D.,  
771 Skiles, S. M., Whicker, C. A., and Zender, C. S.: SNICAR-ADv3: a community  
772 tool for modeling spectral snow albedo, *Geoscientific Model Development*, 14,  
773 7673–7704, 10.5194/gmd-14-7673-2021, 2021.
- 774 Gautam, R., Hsu, N. C., Lau, W. K. M., and Yasunari, T. J.: Satellite observations of  
775 desert dust-induced Himalayan snow darkening, *Geophysical Research Letters*, 40,  
776 988–993, 10.1002/grl.50226, 2013.
- 777 Ge, J. M., Huang, J. P., Xu, C. P., Qi, Y. L., and Liu, H. Y.: Characteristics of Taklimakan  
778 dust emission and distribution: A satellite and reanalysis field perspective, *Journal*  
779 *of Geophysical Research: Atmospheres*, 119, 11,772–711,783,  
780 10.1002/2014jd022280, 2014.
- 781 Gui, K., Yao, W., Che, H., An, L., Zheng, Y., Li, L., Zhao, H., Zhang, L., Zhong, J.,  
782 Wang, Y., and Zhang, X.: Record-breaking dust loading during two mega dust  
783 storm events over northern China in March 2021: aerosol optical and radiative  
784 properties and meteorological drivers, *Atmospheric Chemistry and Physics*, 22,  
785 7905–7932, 10.5194/acp-22-7905-2022, 2022.
- 786 Hadley, O. L. and Kirchstetter, T. W.: Black-carbon reduction of snow albedo, *Nat. Clim.*  
787 *Change*, 2, 437–440, 10.1038/nclimate1433, 2012.
- 788 Han, Y., Wang, T., Tang, J., Wang, C., Jian, B., Huang, Z., and Huang, J.: New insights  
789 into the Asian dust cycle derived from CALIPSO lidar measurements, *Remote*  
790 *Sensing of Environment*, 272, 10.1016/j.rse.2022.112906, 2022.
- 791 He, C., Takano, Y., Liou, K.-N., Yang, P., Li, Q., and Chen, F.: Impact of snow grain  
792 shape and black carbon–snow internal mixing on snow optical properties:  
793 Parameterizations for climate models, *Journal of Climate*, 30, 10019–10036,  
794 10.1175/jcli-d-17-0300.1, 2017.
- 795 He, C., Liou, K. N., Takano, Y., Yang, P., Qi, L., and Chen, F.: Impact of grain shape  
796 and multiple black carbon internal mixing on snow albedo: Parameterization and  
797 radiative effect analysis, *Journal of Geophysical Research: Atmospheres*, 123,  
798 1253–1268, 10.1002/2017jd027752, 2018.
- 799 Huang, H., Qian, Y., He, C., Bair, E. H., and Rittger, K.: Snow albedo feedbacks  
800 enhance snow impurity-induced radiative forcing in the Sierra Nevada,  
801 *Geophysical Research Letters*, 49, e2022GL098102, 10.1029/2022GL098102,  
802 2022.
- 803 Huang, J., Minnis, P., Yi, Y., Tang, Q., Wang, X., Hu, Y., Liu, Z., Ayers, K., Trepte, C.,  
804 and Winker, D.: Summer dust aerosols detected from CALIPSO over the Tibetan  
805 Plateau, *Geophysical Research Letters*, 34, 10.1029/2007gl029938, 2007.
- 806 Huang, J., Minnis, P., Chen, B., Huang, Z., Liu, Z., Zhao, Q., Yi, Y., and Ayers, J. K.:  
807 Long-range transport and vertical structure of Asian dust from CALIPSO and  
808 surface measurements during PACDEX, *Journal of Geophysical Research*, 113,  
809 10.1029/2008jd010620, 2008.
- 810 Huang, J., Wang, T., Wang, W., Li, Z., and Yan, H.: Climate effects of dust aerosols



- 811 over East Asian arid and semiarid regions, *Journal of Geophysical Research:*  
812 *Atmospheres*, 119, 10.1002/2014jd021796, 2014.
- 813 Immerzeel, W. W. and Bierkens, M. F. P.: Asia's water balance, *Nature Geoscience*, 5,  
814 841-842, 10.1038/ngeo1643, 2012.
- 815 Jia, R., Liu, Y., Chen, B., Zhang, Z., and Huang, J.: Source and transportation of summer  
816 dust over the Tibetan Plateau, *Atmospheric Environment*, 123, 210-219,  
817 10.1016/j.atmosenv.2015.10.038, 2015.
- 818 Kang, L., Huang, J., Chen, S., and Wang, X.: Long-term trends of dust events over  
819 Tibetan Plateau during 1961–2010, *Atmospheric Environment*, 125, 188-198,  
820 10.1016/j.atmosenv.2015.10.085, 2016.
- 821 Kraaijenbrink, P. D. A., Bierkens, M. F. P., Lutz, A. F., and Immerzeel, W. W.: Impact  
822 of a global temperature rise of 1.5 degrees Celsius on Asia's glaciers, *Nature*, 549,  
823 257-260, 10.1038/nature23878, 2017.
- 824 Kraaijenbrink, P. D. A., Stigter, E. E., Yao, T., and Immerzeel, W. W.: Climate change  
825 decisive for Asia's snow meltwater supply, *Nature Climate Change*, 11, 591-597,  
826 10.1038/s41558-021-01074-x, 2021.
- 827 Li, Y., Chen, Y., and Li, Z.: Climate and topographic controls on snow phenology  
828 dynamics in the Tianshan Mountains, Central Asia, *Atmospheric Research*, 236,  
829 10.1016/j.atmosres.2019.104813, 2020.
- 830 Li, Y., Kang, S., Zhang, X., Chen, J., Schmale, J., Li, X., Zhang, Y., Niu, H., Li, Z., Qin,  
831 X., He, X., Yang, W., Zhang, G., Wang, S., Shao, L., and Tian, L.: Black carbon  
832 and dust in the Third Pole glaciers: Revaluated concentrations, mass absorption  
833 cross-sections and contributions to glacier ablation, *Science of the Total  
834 Environment*, 789, 147746, 10.1016/j.scitotenv.2021.147746, 2021.
- 835 Li, Y., Kang, S., Zhang, X., Li, C., Chen, J., Qin, X., Shao, L., and Tian, L.: Dust  
836 dominates the summer melting of glacier ablation zones on the northeastern  
837 Tibetan Plateau, *Science of the Total Environment*, 856, 159214,  
838 10.1016/j.scitotenv.2022.159214, 2022.
- 839 Liang, P., Chen, B., Yang, X., Liu, Q., Li, A., Mackenzie, L., and Zhang, D.: Revealing  
840 the dust transport processes of the 2021 mega dust storm event in northern China,  
841 *Science Bulletin*, 67, 21-24, 10.1016/j.scib.2021.08.014, 2021.
- 842 Ménégoz, M., Krinner, G., Balkanski, Y., Boucher, O., Cozic, A., Lim, S., Ginot, P., Laj,  
843 P., Gallée, H., Wagnon, P., Marinoni, A., and Jacobi, H. W.: Snow cover sensitivity  
844 to black carbon deposition in the Himalayas: from atmospheric and ice core  
845 measurements to regional climate simulations, *Atmospheric Chemistry and  
846 Physics*, 14, 4237-4249, 10.5194/acp-14-4237-2014, 2014.
- 847 Meng, L., Yang, X., Zhao, T., He, Q., Lu, H., Mamtimin, A., Huo, W., Yang, F., and Liu,  
848 C.: Modeling study on three-dimensional distribution of dust aerosols during a  
849 dust storm over the Tarim Basin, Northwest China, *Atmospheric Research*, 218,  
850 285-295, 10.1016/j.atmosres.2018.12.006, 2018.
- 851 Ming, J., Xiao, C. D., Wang, F. T., Li, Z. Q., and Li, Y. M.: Grey Tianshan Urumqi  
852 Glacier No.1 and light-absorbing impurities, *Environmental Science and Pollution  
853 Research*, 23, 9549-9558, 10.1007/s11356-016-6182-7, 2016.
- 854 Mishra, S. K., Hayse, J., Veselka, T., Yan, E., Kayastha, R. B., LaGory, K., McDonald,



- 855 K., and Steiner, N.: An integrated assessment approach for estimating the  
856 economic impacts of climate change on River systems: An application to  
857 hydropower and fisheries in a Himalayan River, Trishuli, *Environmental Science*  
858 & Policy, 87, 102-111, 10.1016/j.envsci.2018.05.006, 2018.
- 859 Mishra, S. K., Rupper, S., Kapnick, S., Casey, K., Chan, H. G., Ciraci, E., Haritashya,  
860 U., Hayse, J., Kargel, J. S., Kayastha, R. B., Krakauer, N. Y., Kumar, S. V.,  
861 Lammers, R. B., Maggioni, V., Margulis, S. A., Olson, M., Osmanoglu, B., Qian,  
862 Y., McLarty, S., Rittger, K., Rounce, D. R., Shean, D., Velicogna, I., Veselka, T.  
863 D., and Arendt, A.: Grand challenges of hydrologic modeling for food-energy-  
864 water nexus security in High Mountain Asia, *Frontiers in Water*, 3,  
865 10.3389/frwa.2021.728156, 2021.
- 866 Negi, H. S. and Kokhanovsky, A.: Retrieval of snow grain size and albedo of western  
867 Himalayan snow cover using satellite data, *The Cryosphere*, 5, 831-847,  
868 10.5194/tc-5-831-2011, 2011.
- 869 Notarnicola, C.: Hotspots of snow cover changes in global mountain regions over  
870 2000–2018, *Remote Sensing of Environment.*, 243, 111781,  
871 10.1016/j.rse.2020.111781, 2020.
- 872 Niu, X., Pu, W., Fu, P., Chen, Y., Xing, Y., Wu, D., Chen, Z., Shi, T., Zhou, Y., Wen, H.,  
873 and Wang, X.: Fluorescence characteristics, absorption properties, and radiative  
874 effects of water-soluble organic carbon in seasonal snow across northeastern China,  
875 *Atmospheric Chemistry and Physics*, 22, 14075-14094, 10.5194/acp-22-14075-  
876 2022, 2022.
- 877 Okada, K., Kai, K.: Atmospheric mineral particles collected at Qira in the Taklamakan  
878 Desert, China, *Atmospheric Environment*, 38, 6927-6935,  
879 10.1016/j.atmosenv.2004.03.078, 2004.
- 880 Orsolini, Y., Wegmann, M., Dutra, E., Liu, B., Balsamo, G., Yang, K., de Rosnay, P.,  
881 Zhu, C., Wang, W., Senan, R., and Arduini, G.: Evaluation of snow depth and snow  
882 cover over the Tibetan Plateau in global reanalyses using in situ and satellite  
883 remote sensing observations, *The Cryosphere*, 13, 2221-2239, 10.5194/tc-13-  
884 2221-2019, 2019.
- 885 Painter, T. H., Rittger, K., McKenzie, C., Slaughter, P., Davis, R. E., and Dozier, J.:  
886 Retrieval of subpixel snow covered area, grain size, and albedo from MODIS,  
887 *Remote Sensing of Environment*, 113, 868-879, 10.1016/j.rse.2009.01.001, 2009.
- 888 Painter, T. H., Bryant, A. C., and Skiles, S. M.: Radiative forcing by light absorbing  
889 impurities in snow from MODIS surface reflectance data, *Geophysical Research*  
890 *Letters*, 39, n/a-n/a, 10.1029/2012gl052457, 2012.
- 891 Painter, T. H., Skiles, S. M., Deems, J. S., Brandt, W. T., and Dozier, J.: Variation in  
892 rising limb of colorado river snowmelt runoff hydrograph controlled by dust  
893 radiative forcing in snow, *Geophysical Research Letters*, 45, 797-808,  
894 10.1002/2017gl075826, 2017.
- 895 Patterson, E.M.: Optical properties of the crustal aerosol: Relation to chemical and  
896 physical characteristics, *Journal of Geophysical Research: Atmospheres*, 86, 3236-  
897 3246, 10.1029/JC086iC04p03236, 1981.
- 898 Pu, W., Cui, J., Shi, T., Zhang, X., He, C., and Wang, X.: The remote sensing of radiative



- 899 forcing by light-absorbing particles (LAPs) in seasonal snow over northeastern  
900 China, *Atmospheric Chemistry and Physics*, 19, 9949-9968, 10.5194/acp-19-  
901 9949-2019, 2019.
- 902 Pu, W., Cui, J., Wu, D., Shi, T., Chen, Y., Xing, Y., Zhou, Y., and Wang, X.:  
903 Unprecedented snow darkening and melting in New Zealand due to 2019–2020  
904 Australian wildfires, *Fundamental Research*, 1, 224-231,  
905 10.1016/j.fmre.2021.04.001, 2021.
- 906 Pulliainen, J., Luoju, K., Derksen, C., Mudryk, L., Lemmetyinen, J., Salminen, M.,  
907 Ikonen, J., Takala, M., Cohen, J., Smolander, T., and Norberg, J.: Patterns and  
908 trends of Northern Hemisphere snow mass from 1980 to 2018, 581, 294-298,  
909 s41586-020-2258-0, 2020.
- 910 Qian, Y., Yasunari, T. J., Doherty, S. J., Flanner, M. G., Lau, W. K. M., Ming, J., Wang,  
911 H., Wang, M., Warren, S. G., and Zhang, R.: Light-absorbing particles in snow and  
912 ice: Measurement and modeling of climatic and hydrological impact, *Advances in*  
913 *Atmospheric Sciences*, 32, 64-91, 10.1007/s00376-014-0010-0, 2015.
- 914 Qiu, X., Zeng, Y., and Miao, Q.: Sand-dust storms in China: temporal-spatial  
915 distribution and tracks of source lands, *Journal of Geographical Sciences*. 11, 253–  
916 260, 10.1007/BF02892308, 2001.
- 917 Reveillet, M., Dumont, M., Gascoïn, S., Lafaysse, M., Nabat, P., Ribes, A., Nheili, R.,  
918 Tuzet, F., Menegoz, M., Morin, S., Picard, G., and Ginoux, P.: Black carbon and  
919 dust alter the response of mountain snow cover under climate change, *Nature*  
920 *Communication*, 13, 5279, 10.1038/s41467-022-32501-y, 2022.
- 921 Ricchiazzi, P., Yang, S. R., Gautier, C., and Sowle, D.: SBDART: A research and  
922 teaching software tool for plane-parallel radiative transfer in the Earth's  
923 atmosphere, *Bulletin of the American Meteorological Society*., 79, 2101–2114,  
924 10.1175/1520-0477(1998)079<2101:Sarats>2.0.Co;2, 1998.
- 925 Rittger, K., Painter, T. H., and Dozier, J.: Assessment of methods for mapping snow  
926 cover from MODIS, *Advances in Water Resources*, 51, 367-380,  
927 10.1016/j.advwatres.2012.03.002, 2013.
- 928 Roychoudhury, C., He, C., Kumar, R., McKinnon, J. M., and Arellano, A. F.: On the  
929 relevance of aerosols to snow cover variability over High Mountain Asia,  
930 *Geophysical Research Letters*, 49, 10.1029/2022gl099317, 2022.
- 931 Sang, J., Kim, M.-K., Lau, W. K. M., and Kim, K.-M.: Possible Impacts of snow  
932 darkening effects on the hydrological cycle over western Eurasia and east Asia,  
933 *Atmosphere*, 10, 10.3390/atmos10090500, 2019.
- 934 Sarangi, C., Qian, Y., Rittger, K., Bormann, K. J., Liu, Y., Wang, H., Wan, H., Lin, G.,  
935 and Painter, T. H.: Impact of light-absorbing particles on snow albedo darkening  
936 and associated radiative forcing over high-mountain Asia: high-resolution WRF-  
937 Chem modeling and new satellite observations, *Atmospheric Chemistry and*  
938 *Physics*, 19, 7105-7128, 10.5194/acp-19-7105-2019, 2019.
- 939 Sarangi, C., Qian, Y., Rittger, K., Ruby Leung, L., Chand, D., Bormann, K. J., and  
940 Painter, T. H.: Dust dominates high-altitude snow darkening and melt over high-  
941 mountain Asia, *Nature Climate Change*, 10, 1045-1051, 10.1038/s41558-020-  
942 00909-3, 2020.



- 943 Schmale, J., Flanner, M., Kang, S. C., Sprenger, M., Zhang, Q. G., Guo, J. M., Li, Y.,  
944 Schwikowski, M., and Farinotti, D.: Modulation of snow reflectance and  
945 snowmelt from Central Asian glaciers by anthropogenic black carbon, *Scientific*  
946 *Reports*, 7, 40501, 10.1038/srep40501, 2017.
- 947 Siegmund., A. and Menz., G.: Fernes nah gebracht – satelliten- und luftbildeinsatz zur  
948 analyse von umweltveränderungen im geographieunterricht, *Geographie und*  
949 *Schule*, 154, 2–10, 2005.
- 950 Shao, Y. and Dong, C. H.: A review on East Asian dust storm climate, modelling and  
951 monitoring, *Global and Planetary Change*, 52, 1–22,  
952 10.1016/j.gloplacha.2006.02.011, 2006.
- 953 She, J., Zhang, Y., Li, X., and Feng, X.: Spatial and temporal characteristics of snow  
954 cover in the Tizinafu watershed of the Western Kunlun Mountains, *Remote*  
955 *Sensing*, 7, 3426–3445, 10.3390/rs70403426, 2015.
- 956 Shi, T., Pu, W., Zhou, Y., Cui, J., Zhang, D., and Wang, X.: Albedo of black carbon-  
957 contaminated snow across Northwestern China and the validation with model  
958 simulation, *Journal of Geophysical Research: Atmospheres*, 125,  
959 10.1029/2019jd032065, 2020.
- 960 Shi, T., Cui, J., Chen, Y., Zhou, Y., Pu, W., Xu, X., Chen, Q., Zhang, X., and Wang, X.:  
961 Enhanced light absorption and reduced snow albedo due to internally mixed  
962 mineral dust in grains of snow, *Atmospheric Chemistry and Physics*, 21, 6035-  
963 6051, 10.5194/acp-21-6035-2021, 2021.
- 964 Shi, T., Cui, J., Wu, D., Xing, Y., Chen, Y., Zhou, Y., Pu, W., and Wang, X.: Snow albedo  
965 reductions induced by the internal/external mixing of black carbon and mineral  
966 dust, and different snow grain shapes across northern China, *Environmental*  
967 *Research*, 208, 112670, 10.1016/j.envres.2021.112670, 2022a.
- 968 Shi, T., Chen, Y., Xing, Y., Niu, X., Wu, D., Cui, J., Zhou, Y., Pu, W., and Wang, X.:  
969 Assessment of the combined radiative effects of black carbon in the atmosphere  
970 and snowpack in the Northern Hemisphere constrained by surface observations,  
971 *Environmental Science: Atmospheres*, 2, 702–713, 10.1039/d2ea00005a, 2022b.
- 972 Shi, Z., Xie, X., Li, X., Yang, L., Xie, X., Lei, J., Sha, Y., and Liu, X.: Snow-darkening  
973 versus direct radiative effects of mineral dust aerosol on the Indian summer  
974 monsoon onset: role of temperature change over dust sources, *Atmospheric*  
975 *Chemistry and Physics*, 19, 1605–1622, 10.5194/acp-19-1605-2019, 2019.
- 976 Skiles, S. M. and Painter, T.: Daily evolution in dust and black carbon content, snow  
977 grain size, and snow albedo during snowmelt, *Rocky Mountains, Colorado,*  
978 *Journal of Glaciology*, 63, 118–132, 10.1017/jog.2016.125, 2016.
- 979 Skiles, S. M., Flanner, M., Cook, J. M., Dumont, M., and Painter, T. H.: Radiative  
980 forcing by light-absorbing particles in snow, *Nature Climate Change*, 8, 964–971,  
981 10.1038/s41558-018-0296-5, 2018a.
- 982 Skiles, S. M., Mallia, D. V., Hallar, A. G., Lin, J. C., Lambert, A., Petersen, R., and  
983 Clark, S.: Implications of a shrinking Great Salt Lake for dust on snow deposition  
984 in the Wasatch Mountains, UT, as informed by a source to sink case study from  
985 the 13–14 April 2017 dust event, *Environmental Research Letters*, 13,  
986 10.1088/1748-9326/aaefd8, 2018b.



- 987 Sun, J., Zhang, M., and Liu, T.: Spatial and temporal characteristics of dust storms in  
988 China and its surrounding regions, 1960-1999: Relations to source area and  
989 climate, *Journal of Geophysical Research: Atmospheres*, 106, 10325-10333,  
990 10.1029/2000jd900665, 2001.
- 991 Tang, W., Dai, T., Cheng, Y., Wang, S., and Liu, Y.: A study of a severe spring dust event  
992 in 2021 over east Asia with WRF-Chem and multiple platforms of observations,  
993 *Remote Sensing*, 14, 10.3390/rs14153795, 2022.
- 994 Teillet, P. M., Guindon, B., and Goodenough, D. G.: On the slope-aspect correction of  
995 multispectral scanner data, *Canadian Journal of Remote Sensing*, 8, 84-106,  
996 10.1080/07038992.1982.10855028, 1982.
- 997 Usha, K. H., Nair, V. S., and Babu, S. S.: Deciphering the role of aerosol-induced snow  
998 albedo feedback on dust emission over the Tibetan Plateau, *Journal of Geophysical  
999 Research: Atmospheres*, 127, 10.1029/2021jd036384, 2022.
- 1000 Wake, C. P., Mayewski, P. A., Li, Z., Han, J., and Qin, D.: Modern eolian dust deposition  
1001 in central Asia, *Tellus B: Chemical and Physical Meteorology*, 46,  
1002 10.3402/tellusb.v46i3.15793, 1994.
- 1003 Wang, X., Huang, J., Ji, M., and Higuchi, K.: Variability of East Asia dust events and  
1004 their long-term trend, *Atmospheric Environment*, 42, 3156-3165,  
1005 10.1016/j.atmosenv.2007.07.046, 2008.
- 1006 Wang, X., Doherty, S. J., and Huang, J.: Black carbon and other light-absorbing  
1007 impurities in snow across Northern China, *Journal of Geophysical Research:  
1008 Atmospheres*, 118, 1471-1492, 10.1029/2012jd018291, 2013.
- 1009 Wang, X., Pu, W., Ren, Y., Zhang, X., Zhang, X., Shi, J., Jin, H., Dai, M., and Chen, Q.:  
1010 Observations and model simulations of snow albedo reduction in seasonal snow  
1011 due to insoluble light-absorbing particles during 2014 Chinese survey,  
1012 *Atmospheric Chemistry and Physics*, 17, 2279-2296, 10.5194/acp-17-2279-2017,  
1013 2017.
- 1014 Wang, X., Wei, H., Liu, J., Xu, B., Wang, M., Ji, M., and Jin, H.: Quantifying the light  
1015 absorption and source attribution of insoluble light-absorbing particles on Tibetan  
1016 Plateau glaciers between 2013 and 2015, *The Cryosphere*, 13, 309-324,  
1017 10.5194/tc-13-309-2019, 2019.
- 1018 Wei, T., Dong, Z., Kang, S., Qin, X., and Guo, Z.: Geochemical evidence for sources  
1019 of surface dust deposited on the Laohugou glacier, Qilian Mountains, *Applied  
1020 Geochemistry*, 79, 1-8, 10.1016/j.apgeochem.2017.01.024, 2017.
- 1021 Wiscombe, W. J. and Warren, S. G.: A model for the spectral albedo of snow .1. Pure  
1022 snow, *Journal of the Atmospheric Sciences*, 37, 2712-2733,  
1023 10.1175/15200469(1980)037<2712:Amftsa>2.0.Co;2, 1980.
- 1024 Wu, D., Liu, J., Wang, T., Niu, X., Chen, Z., Wang, D., Zhang, X., Ji, M., Wang, X.,  
1025 and Pu, W.: Applying a dust index over North China and evaluating the  
1026 contribution of potential factors to its distribution, *Atmospheric Research*, 254,  
1027 10.1016/j.atmosres.2021.105515, 2021.
- 1028 Wu, G., Yao, T., Xu, B., Tian, L., Zhang, C., and Zhang, X.: Dust concentration and  
1029 flux in ice cores from the Tibetan Plateau over the past few decades, *Tellus B:  
1030 Chemical and Physical Meteorology*, 62, 10.1111/j.1600-0889.2010.00457.x,





- 1031 2010.
- 1032 Xu, J., Kang, S., Hou, S., Zhang, Q., Huang, J., Xiao, C., Ren, J., and Qin, D.:  
1033 Characterization of contemporary aeolian dust deposition on mountain glaciers of  
1034 western China, *Sci. Cold Arid Reg*, 8, 0009-0021, 2016.
- 1035 Yang, L., Shi, Z., Xie, X., Li, X., Liu, X., and An, Z.: Seasonal changes in East Asian  
1036 monsoon-westerly circulation modulated by the snow-darkening effect of mineral  
1037 dust, *Atmospheric Research*, 279, 10.1016/j.atmosres.2022.106383, 2022.
- 1038 Yao, T., Thompson, L., Yang, W., Yu, W., Gao, Y., Guo, X., Yang, X., Duan, K., Zhao,  
1039 H., Xu, B., Pu, J., Lu, A., Xiang, Y., Kattel, D. B., and Joswiak, D.: Different  
1040 glacier status with atmospheric circulations in Tibetan Plateau and surroundings,  
1041 *Nature Climate Change*, 2, 663-667, 10.1038/nclimate1580, 2012.
- 1042 Yao, T., Xue, Y., Chen, D., Chen, F., Thompson, L., Cui, P., Koike, T., Lau, W. K. M.,  
1043 Lettenmaier, D., Mosbrugger, V., Zhang, R., Xu, B., Dozier, J., Gillespie, T., Gu,  
1044 Y., Kang, S., Piao, S., Sugimoto, S., Ueno, K., Wang, L., Wang, W., Zhang, F.,  
1045 Sheng, Y., Guo, W., Ailikun, Yang, X., Ma, Y., Shen, S. S. P., Su, Z., Chen, F.,  
1046 Liang, S., Liu, Y., Singh, V. P., Yang, K., Yang, D., Zhao, X., Qian, Y., Zhang, Y.,  
1047 and Li, Q.: Recent Third Pole's rapid warming accompanies cryospheric melt and  
1048 water cycle intensification and interactions between monsoon and environment:  
1049 Multidisciplinary approach with observations, modeling, and analysis, *Bulletin of  
1050 the American Meteorological Society*, 100, 423-444, 10.1175/bams-d-17-0057.1,  
1051 2019.
- 1052 Yuan, T., Chen, S., Huang, J., Wu, D., Lu, H., Zhang, G., Ma, X., Chen, Z., Luo, Y., and  
1053 Ma, X.: Influence of dynamic and thermal forcing on the meridional transport of  
1054 Taklimakan desert dust in spring and summer, *Journal of Climate*, 32, 749-767,  
1055 10.1175/jcli-d-18-0361.1, 2018.
- 1056 Zhang, B., Tsunekawa, A., and Tsubo, M.: Contributions of sandy lands and stony  
1057 deserts to long-distance dust emission in China and Mongolia during 2000–2006,  
1058 *Global and Planetary Change*, 60, 487-504, 10.1016/j.gloplacha.2007.06.001,  
1059 2008.
- 1060 Zhang, X., Li, Z. Q., You, X. N., She, Y. Y., Song, M. Y., and Zhou, X.: Light-Absorbing  
1061 Impurities on Urumqi Glacier No.1 in Eastern Tien Shan: Concentrations and  
1062 Implications for Radiative Forcing Estimates During the Ablation Period,  
1063 *Frontiers in Earth Science*, 9, 2296-6463, 10.3389/feart.2021.524963, 2021.
- 1064 Zhang, Y., Kang, S., Sprenger, M., Cong, Z., Gao, T., Li, C., Tao, S., Li, X., Zhong, X.,  
1065 Xu, M., Meng, W., Neupane, B., Qin, X., and Sillanpää, M.: Black carbon and  
1066 mineral dust in snow cover on the Tibetan Plateau, *The Cryosphere*, 12, 413-431,  
1067 10.5194/tc-12-413-2018, 2018.
- 1068 Zhang, Y., Gao, T., Kang, S., Sprenger, M., Tao, S., Du, W., Yang, J., Wang, F., and  
1069 Meng, W.: Effects of black carbon and mineral dust on glacial melting on the Muz  
1070 Taw glacier, Central Asia, *Science of the Total Environment*, 740, 140056,  
1071 10.1016/j.scitotenv.2020.140056, 2020.
- 1072 Zhang, Y., Gao, T., Kang, S., Shanguan, D., and Luo, X.: Albedo reduction as an  
1073 important driver for glacier melting in Tibetan Plateau and its surrounding areas,  
1074 *Earth-Science Reviews*, 220, 10.1016/j.earscirev.2021.103735, 2021.



1075 Zhao, X., Huang, K., Fu, J. S., and Abdullaev, S. F.: Long-range transport of Asian dust  
1076 to the Arctic: identification of transport pathways, evolution of aerosol optical  
1077 properties, and impact assessment on surface albedo changes, *Atmospheric*  
1078 *Chemistry and Physics*, 22, 10389-10407, 10.5194/acp-22-10389-2022, 2022.  
1079 Zhu, L., Ma, G., Zhang, Y., Wang, J., Tian, W., and Kan, X.: Accelerated decline of  
1080 snow cover in China from 1979 to 2018 observed from space, *Science of the Total*  
1081 *Environment*, 814, 152491, 10.1016/j.scitotenv.2021.152491, 2022.  
1082  
1083  
1084